

Fast simulation of Gaussian random fields with flexible correlation models in Euclidean spaces

Moreno Bevilacqua*

Xavier Emery†

Francisco Cuevas-Pacheco‡

Abstract

The efficient simulation of Gaussian random fields with flexible correlation structures is fundamental in spatial statistics, machine learning, and uncertainty quantification. In this work, we revisit the *spectral turning-bands* (STB) method as a versatile and scalable framework for simulating isotropic Gaussian random fields with a broad range of covariance models.

Beyond the classical Matérn family, we show that the STB approach can be extended to two recent and flexible correlation classes that generalize the Matérn model: the *Kummer–Tricomi* model, which allows for polynomially decaying correlations and long-range dependence, and the *Gauss–Hypergeometric* model, which admits compactly supported correlations, including the Generalized Wendland family as a special case.

We derive exact stochastic representations for both families: a *Beta–prime mixture* formulation for the Kummer–Tricomi model and complementary *Beta–* and *Gasper–mixture* representations for the Gauss–Hypergeometric model. These formulations enable exact, numerically stable, and computationally efficient simulation with linear complexity in the number of spectral components. Numerical experiments confirm the accuracy and computational stability of the proposed algorithms across a wide range of parameter configurations, demonstrating their practical viability for large-scale spatial modeling. As an application, we use the proposed STB simulators to perform parametric bootstrap for standard error estimation and model selection under weighted pairwise composite likelihood in the analysis of a large climate dataset.

1 Introduction

1.1 Motivation

Gaussian random fields (RFs) play a central role in spatial statistics, geostatistics, machine learning, signal processing, and uncertainty quantification. A Gaussian RF is fully characterized by its mean function and by its covariance structure, which determines both the smoothness and the spatial dependence of the field. In many applications, from spatial interpolation to Bayesian inverse problems, fast simulation from a given covariance model is essential both for inference and for propagating uncertainty through complex models. Fast Gaussian RF simulation is also fundamental for likelihood-free inference techniques such as Approximate Bayesian Computation (Sisson et al., 2018) and simulation-based amortized methods (Zammit-Mangion et al., 2025), as well as

*Facultad de Ingeniería y Ciencias, Universidad Adolfo Ibáñez, Chile; Dipartimento di Scienze Ambientali, Informatica e Statistica, Università Ca' Foscari, Italy.

†Department of Mining Engineering, Universidad de Chile, Santiago, Chile; Advanced Mining Technology Center, Universidad de Chile, Santiago, Chile.

‡Departamento de Matemática, Universidad Técnica Federico Santa María, Chile.

for simulation-based hypothesis testing, for instance the Global Rank Envelope Test (Myllymäki et al., 2016).

Furthermore, the simulation of non-Gaussian RFs derived from latent Gaussian RFs is of importance in many applied contexts, such as spatial extremes, environmental risk assessment, and subsurface modeling. Examples include RFs constructed through transformations of one or more Gaussian RFs—such as the general class of Gaussian copulas (Guido Masarotto and Varin, 2012), truncated Gaussian and plurigaussian (Armstrong et al., 2011), substitution (Emery, 2008), chi-squared (Adler, 1981), non-central chi-squared (Emery, 2007), Tukey- g -and- h (Xu and Genton, 2017), Weibull (Bevilacqua et al., 2020) and Poisson-based (Morales-Navarrete et al., 2024) RFs.

1.2 Review of existing methods

One of the earliest and most widely used method for simulating a Gaussian RF with an arbitrary covariance function at a given set of spatial locations is the *Cholesky method* (Ripley, 1987). This approach relies on the Cholesky decomposition of the covariance matrix and has a computational cost of $O(N^3)$, where N denotes the number of spatial locations. Consequently, the method becomes computationally prohibitive for large spatial domains. To address this limitation, numerous approaches have been developed to exploit structural properties of the covariance matrix and thereby reduce the computational burden.

For instance, the *circulant embedding* method (Dietrich and Newsam, G.N., 1993; Chan and Wood, 1997) exploits the relationship between circulant matrices and the Fast Fourier Transform (FFT), obtained by embedding the regular grid into a torus. This yields a method that requires only $O(N \log N)$ operations thanks to the FFT algorithm. However, it requires the spatial locations to lie on a regular grid of a Euclidean space. This restriction makes it less appealing for practical applications, where observation locations are often irregular. Moreover, additional corrections are necessary when the discrete spectrum of the covariance matrix exhibits negative values, which may occur for stationary covariance models with a smooth behavior at the origin (Chilès and Delfiner, 2012).

A different class of methods can handle large datasets on irregular grids through the *Vecchia approximation* (Vecchia, 1988) and its extensions (Datta et al., 2016; Katsfuss and Guinness, 2021). These approaches exploit the conditional independence structure implied by a sparse approximation of the precision matrix of a Gaussian RF. By conditioning each location on a small number of neighbors $m \ll N$, the resulting sparse factorization allows sequential simulation with a computational cost of order $O(Nm^2)$. The ordering of the locations (e.g., maximum–minimum or middle–out ordering) and the selection of neighbors strongly affect the accuracy of the approximation. Vecchia-based methods are particularly effective for covariance models whose precision matrices exhibit local dependence, such as the Matérn class, although their accuracy may deteriorate for models with compact support, where the precision matrix tends to be dense despite the sparsity of the covariance matrix (Porcu et al., 2024).

An alternative approach, specifically designed for the Matérn model and capable of achieving both high accuracy and computational efficiency, is the *SPDE-INLA* framework (Lindgren et al., 2011). In this method, the continuous field is represented on a finite element mesh, resulting in a Gaussian Markov RF whose precision matrix is sparse by construction. This sparsity allows simulations to be performed by solving sparse linear systems instead of manipulating dense covariance matrices, reducing the computational cost approximately $O(N^{3/2})$ or even $O(N)$, depending on the mesh topology and spatial dimension.

Other alternative simulation strategies that can be applied to any covariance function and are based on Markov chain Monte Carlo (MCMC) methods have also been explored. Gibbs sampling (Geman and Geman, 1984) and Metropolis–Hastings (Hastings, 1970) methods are particularly appealing for irregularly distributed locations. However, they are generally inefficient for large-scale simulations, as they require a large number of iterations to ensure convergence, can exhibit numerical instabilities, and still rely on sampling from conditional Gaussian distributions involving the inverse of the covariance matrix.

For compactly supported correlations functions, methods based on the Cholesky factorization of sparse covariance matrices (Davis, 2006; Duff et al., 1989), can be effective for simulation goals. However, these methods require the covariance matrix to be highly sparse to achieve significant computational gains and are therefore applicable only in limited settings.

Another widely used and conceptually different approach for simulating Gaussian RFs in Euclidean spaces is the continuous spectral method (Shinozuka, 1971; Shinozuka and Jan, 1972), which can be applied to any stationary covariance function and arbitrary sampling configurations, provided that the Fourier transform of the covariance function is available.

This method can be regarded as a particular case of the more general *turning-bands* approach proposed by Matheron (1973), which relies on spreading a one-dimensional RF over the multidimensional Euclidean space. In this context, the one-dimensional field corresponds to a cosine wave in Shinozuka’s spectral method, which will be referred to here as the “spectral turning–bands” (STB) method, following the terminology of Mantoglou and Wilson (1987) and Emery et al. (2016).

The STB method is particularly attractive because it requires only the simulation of univariate processes along randomly oriented lines, making it both simple and computationally efficient. The number of such random lines, denoted by L , controls the convergence of the simulation to a Gaussian RF: higher values of L lead to a better central limit approximation, albeit at the cost of increased computation. The overall computational cost scales linearly with both the number of spatial locations and L , that is, $O(NL)$.

1.3 Contribution

This work focuses on applying the STB method to the simulation of Gaussian RFs in Euclidean spaces with *flexible isotropic correlation models*. By *flexible models*, we refer to parametric correlation families that allow continuous control over the smoothness of the Gaussian RF.

The Matérn (\mathcal{M}) family (Stein, 1999; Porcu et al., 2024) is widely regarded as the benchmark model in spatial statistics due to its interpretable parameters and explicit control of mean-square differentiability. However, as noted in Porcu et al. (2024), the \mathcal{M} model presents two well-known limitations: (i) the assumption of global support, and (ii) the exponential correlation decay, which may be overly restrictive for modeling long-range dependence.

To overcome these limitations, two recent covariance functions that generalize the \mathcal{M} class have been proposed:

1. The *Gauss–Hypergeometric* (\mathcal{GH}) model (Emery and Alegría, 2022; Bevilacqua et al., 2025a), which defines a broad class of compactly supported correlations including, as special cases, the celebrated Generalized Wendland family (Gneiting, 2002; Bevilacqua et al., 2019). This class preserves the smoothness parameterization of the \mathcal{M} model while introducing an additional shape parameter. Its compact support is a desirable property from a computational perspective, as it yields sparse covariance matrices.

2. The *Kummer–Tricomi* (\mathcal{K}) (or confluent hypergeometric) model (Ma and Bhadra, 2022), which introduces an additional tail parameter allowing for polynomial decay while maintaining smoothness flexibility in all spatial dimensions.

Both models can therefore be viewed as generalizations of the \mathcal{M} class, enhancing its flexibility in opposite directions: the \mathcal{GH} model toward compactly supported correlations, and the \mathcal{K} model toward heavy-tailed, long-range dependence.

While STB simulation for the \mathcal{M} model is classical and well understood (Emery and Lantuéjoul, 2006), in this work we extend the STB framework to the \mathcal{K} and \mathcal{GH} families. For both families, the application of the STB method faces the difficulty of sampling from the spectral density, for which no exact solution (except specific cases, as in Arroyo and Emery (2021)) has been proposed to date due to the intricate expression of this density that involves special (hypergeometric) functions. To solve this problem, we derive exact spectral representations and corresponding stochastic samplers that enable STB simulation without numerical integration or approximation, allowing efficient large-scale generation of isotropic Gaussian RFs under flexible correlation structures. In particular:

- we show that the \mathcal{K} kernel admits an exact spectral representation enabling direct STB sampling through a Beta–prime Gaussian mixture;
- we demonstrate that STB sampling can also be extended to the \mathcal{GH} class by exploiting two alternative representations involving Beta and Gasper mixtures.

The proposed algorithms provide a unified stochastic framework for the fast simulation of Gaussian RFs with \mathcal{M} , \mathcal{K} , and \mathcal{GH} covariance functions for a large number of spatial locations (up to millions). They have been implemented in the function `GeoSimapprox` of the R package `GeoModels` (Bevilacqua et al., 2025b), which allows for the simulation of Gaussian and a wide range of non-Gaussian spatial fields with \mathcal{M} , \mathcal{K} , and \mathcal{GH} underlying correlation models.

Two numerical studies illustrate the proposed methodology. First, we conduct a comprehensive simulation study to assess the accuracy of the STB algorithms for both the \mathcal{GH} and \mathcal{K} models across a wide range of parameter configurations, comparing empirical semivariograms with their theoretical counterparts. Second, we analyze a large climate dataset and show how the proposed STB simulators can be used to perform parametric bootstrap for the computation of standard errors and model selection criteria under weighted pairwise composite likelihood (Caamaño-Carrillo et al., 2024), for Gaussian and transformed Gaussian random fields with \mathcal{M} , \mathcal{K} and Generalized Wendland correlation functions.

1.4 Outline

The remainder of the paper is organized as follows. Section 2 recalls the spectral representation of stationary Gaussian RFs and the spectral turning–bands (STB) framework. Section 3 reviews the \mathcal{M} correlation model and its STB sampler. Section 4 develops the \mathcal{K} model, its spectral representation, and the associated STB algorithms. Section 5 introduces the \mathcal{GH} family, including the Beta– and Gasper–mixture formulations and the corresponding STB algorithms. Section 6 reports numerical experiments assessing the accuracy and stability of the proposed samplers. Section 7 presents an application to climate data based on weighted composite likelihood and parametric bootstrap. Section 8 concludes with a discussion and perspectives for future work.

2 Spectral representation and spectral turning–bands simulation

Let $\{Z(\mathbf{s}) : \mathbf{s} \in D\}$ be a real, zero-mean stationary Gaussian RF defined on a bounded domain $D \subset \mathbb{R}^d$, with stationary covariance

$$C(\mathbf{h}) = \text{Cov}(Z(\mathbf{s}), Z(\mathbf{s} + \mathbf{h})), \quad \mathbf{h} \in \mathbb{R}^d,$$

and variance $\sigma^2 := C(\mathbf{0})$. The corresponding correlation function is $\phi(\mathbf{h}) = C(\mathbf{h})/\sigma^2$ with $\phi(\mathbf{0}) = 1$.

By Bochner's theorem, any continuous positive-semidefinite function $C : \mathbb{R}^d \rightarrow \mathbb{C}$ admits the representation (A. M. Yaglom, 1987)

$$C(\mathbf{h}) = \int_{\mathbb{R}^d} e^{i\boldsymbol{\omega} \cdot \mathbf{h}} F(d\boldsymbol{\omega}), \quad (1)$$

where i is the imaginary unit, \cdot is the usual scalar product on \mathbb{R}^d , and F is a finite nonnegative symmetric measure on \mathbb{R}^d . If F has a density f_C , then

$$C(\mathbf{h}) = \int_{\mathbb{R}^d} e^{i\boldsymbol{\omega} \cdot \mathbf{h}} f_C(\boldsymbol{\omega}) d\boldsymbol{\omega}, \quad f_C(\boldsymbol{\omega}) \geq 0, \quad \int_{\mathbb{R}^d} f_C(\boldsymbol{\omega}) d\boldsymbol{\omega} = \sigma^2.$$

For a real-valued RF, $C(\mathbf{h}) = C(-\mathbf{h})$, so that

$$C(\mathbf{h}) = \int_{\mathbb{R}^d} \cos(\boldsymbol{\omega} \cdot \mathbf{h}) f_C(\boldsymbol{\omega}) d\boldsymbol{\omega}.$$

Henceforth, we denote by f the normalized spectral density of the correlation function ϕ , i.e.

$$f(\boldsymbol{\omega}) := \frac{1}{\sigma^2} f_C(\boldsymbol{\omega}), \quad \int_{\mathbb{R}^d} f(\boldsymbol{\omega}) d\boldsymbol{\omega} = 1,$$

and hence

$$\phi(\mathbf{h}) = \int_{\mathbb{R}^d} \cos(\boldsymbol{\omega} \cdot \mathbf{h}) f(\boldsymbol{\omega}) d\boldsymbol{\omega}. \quad (2)$$

For an isotropic RF, $\phi(\mathbf{h}) = \phi(x)$ with $x = \|\mathbf{h}\|$ and the spectral density depends only on $r = \|\boldsymbol{\omega}\|$, that is $f(\boldsymbol{\omega}) = g_R(r)$ for some radial function g_R . Integrating (2) over directions gives the Schoenberg representation (Schoenberg, 1938):

$$\phi(x) = \int_0^\infty \Omega_d(xr) |\mathbb{S}^{d-1}| r^{d-1} g_R(r) dr, \quad x \geq 0, \quad (3)$$

where $|\mathbb{S}^{d-1}| = \frac{2\pi^{d/2}}{\Gamma(d/2)}$ is the surface area of the $(d-1)$ -dimensional unit sphere and

$$\Omega_d(x) = \Gamma\left(\frac{d}{2}\right) \left(\frac{2}{x}\right)^{d/2-1} J_{d/2-1}(x), \quad x > 0,$$

with J_ν the Bessel function of the first kind of order ν . We denote by Φ_d the class of continuous isotropic positive-definite functions on \mathbb{R}^d with $\phi(0) = 1$; these classes are nested as $\Phi_1 \supset \Phi_2 \supset \dots \supset \Phi_\infty := \bigcap_{d \geq 1} \Phi_d$.

Let $\boldsymbol{\Omega} \in \mathbb{R}^d$ denote a random *frequency vector* with density $f(\boldsymbol{\omega}) = g_R(\|\boldsymbol{\omega}\|)$ normalized so that

$$\int_{\mathbb{R}^d} f(\boldsymbol{\omega}) d\boldsymbol{\omega} = |\mathbb{S}^{d-1}| \int_0^\infty r^{d-1} g_R(r) dr = 1.$$

The random variable $R = \|\boldsymbol{\Omega}\|$ is the *spectral radius*. Its density is

$$f_R(r) = |\mathbb{S}^{d-1}| r^{d-1} g_R(r), \quad r \geq 0. \quad (4)$$

With this normalization,

$$\phi(\|\mathbf{h}\|) = \mathbb{E}[\cos(\boldsymbol{\Omega} \cdot \mathbf{h})], \quad \mathbf{h} \in \mathbb{R}^d. \quad (5)$$

Writing $\boldsymbol{\Omega} = R\boldsymbol{\Theta}$ with R distributed as in (4) and $\boldsymbol{\Theta} \sim \text{Unif}(\mathbb{S}^{d-1})$ independent of R , we obtain a factorization that naturally leads to spectral simulation schemes. In particular, the spectral turning-bands (STB) method exploits the probabilistic representation (5) by approximating the expectation with a Monte Carlo average.

An approximately Gaussian RF with isotropic covariance $\sigma^2 \phi(x)$ can be represented as (Lantuéjoul, 2002)

$$\tilde{Z}_L(\mathbf{s}) = \sigma \sum_{\ell=1}^L \sqrt{\frac{-2 \ln(\varepsilon_\ell)}{L}} \cos(\boldsymbol{\Omega}_\ell \cdot \mathbf{s} + \Phi_\ell), \quad \mathbf{s} \in D, \quad (6)$$

where

$$\varepsilon_\ell \stackrel{\text{i.i.d.}}{\sim} \text{Unif}(0, 1), \quad \boldsymbol{\Omega}_\ell \stackrel{\text{i.i.d.}}{\sim} f(\boldsymbol{\omega}) = g_R(\|\boldsymbol{\omega}\|), \quad \Phi_\ell \stackrel{\text{i.i.d.}}{\sim} \text{Unif}(0, 2\pi), \quad \ell = 1, \dots, L.$$

Each cosine term represents a random wave with direction orthogonal to $\boldsymbol{\Omega}_\ell$ and phase Φ_ℓ , so \tilde{Z}_L is a superposition of L independent spectral components. Following Allard et al. (2020), the random variable ε_ℓ in (6) is introduced so that, for each spectral component ℓ and location \mathbf{s} , the factor $\sqrt{-2 \ln(\varepsilon_\ell)} \cos(\boldsymbol{\Omega}_\ell \cdot \mathbf{s} + \Phi_\ell)$ has a standard Gaussian distribution (Box and Muller, 1958); hence \tilde{Z}_L has marginal Gaussian distribution with variance σ^2 .

By construction,

$$\mathbb{E}[\tilde{Z}_L(\mathbf{s})] = 0, \quad \mathbf{s} \in D,$$

and, for any $\mathbf{s}, \mathbf{t} \in D$,

$$\mathbb{E}[\tilde{Z}_L(\mathbf{s}) \tilde{Z}_L(\mathbf{t})] = \sigma^2 \phi(\|\mathbf{s} - \mathbf{t}\|).$$

Moreover, owing to the central limit theorem, \tilde{Z}_L converges in finite-dimensional distributions to an exact Gaussian RF as $L \rightarrow \infty$, with mean-square error $O(L^{-1/2})$ in the Monte Carlo approximation of the covariance.

Since $f(\boldsymbol{\omega}) = g_R(\|\boldsymbol{\omega}\|)$ depends only on the modulus,

$$\boldsymbol{\Omega} = R\boldsymbol{\Theta}, \quad R \geq 0, \quad \boldsymbol{\Theta} \sim \text{Unif}(\mathbb{S}^{d-1}), \quad R \perp\!\!\!\perp \boldsymbol{\Theta}.$$

Thus, isotropic frequencies are obtained by sampling R from $f_R(r)$ (a model-specific distribution), sampling $\boldsymbol{\Theta} \sim \text{Unif}(\mathbb{S}^{d-1})$ and setting $\boldsymbol{\Omega} = R\boldsymbol{\Theta}$. This decomposition separates the radial and angular components and allows model-dependent samplers for R .

Given $\phi \in \Phi_d$ with radial spectral density g_R and sill σ^2 , the generic STB algorithm is:

1. Choose the number of spectral components L .
2. For each $\ell = 1, \dots, L$:
 - (a) Sample $R_\ell \sim f_R$;

- (b) Sample $\boldsymbol{\Theta}_\ell \sim \text{Unif}(\mathbb{S}^{d-1})$ and set $\boldsymbol{\Omega}_\ell = R_\ell \boldsymbol{\Theta}_\ell$;
- (c) Sample $\Phi_\ell \sim \text{Unif}(0, 2\pi)$;
- (d) Sample $\varepsilon_\ell \sim \text{Unif}(0, 1)$;

3. Compute $\tilde{Z}_L(\mathbf{s})$ via (6) for all $\mathbf{s} \in D$.

The computational cost scales as $O(L|D|)$, with straightforward parallelization across frequencies and spatial locations.

3 The Matérn correlation model

In this section, we review the Matérn class \mathcal{M} (Stein, 1999; Porcu et al., 2024) and discuss how fast simulations based on this model can be performed using the STB method. The \mathcal{M} class is one of the most widely used families of isotropic correlation functions, providing a simple and interpretable control over both the smoothness and the spatial range of the RF. For parameters $\nu > 0$ (smoothness) and $\alpha > 0$ (scale), we adopt the standard parameterization (Matérn, 1986):

$$\mathcal{M}_{\nu,\alpha}(x) = \frac{2^{1-\nu}}{\Gamma(\nu)} \left(\frac{x}{\alpha}\right)^\nu K_\nu\left(\frac{x}{\alpha}\right), \quad x \geq 0, \quad (7)$$

where K_ν denotes the modified Bessel function of the second kind.

The parameter ν controls the mean-square differentiability of the RF: for any integer $k > 0$, the field is k times mean-square differentiable if and only if $\nu > k$. The \mathcal{M} model belongs to Φ_∞ and is thus positive semidefinite in any Euclidean dimension.

The isotropic radial spectral density associated with (7) in \mathbb{R}^d , normalized so that it integrates to one on \mathbb{R}^d , is

$$g_R^{\mathcal{M}}(r) = \frac{\Gamma(\nu + \frac{d}{2}) \alpha^d}{\Gamma(\nu) \pi^{d/2}} (1 + \alpha^2 r^2)^{-(\nu+d/2)}, \quad r \geq 0, \quad (8)$$

so that the full spectral density of the correlation function is $f(\boldsymbol{\omega}) = g_R^{\mathcal{M}}(\|\boldsymbol{\omega}\|)$.

A key property of the \mathcal{M} model is that its spectral distribution admits an exact Gaussian scale-mixture representation, which enables direct frequency sampling for STB simulation. Let

$$T \sim \text{Gamma}(\nu, 1), \quad \mathbf{Z} \sim \mathcal{N}(\mathbf{0}, I_d), \quad T \perp\!\!\!\perp \mathbf{Z},$$

and define

$$\boldsymbol{\Omega} = \frac{1}{\alpha \sqrt{2T}} \mathbf{Z} \in \mathbb{R}^d. \quad (9)$$

Then $\boldsymbol{\Omega}$ follows a multivariate Student- t distribution (Fang et al., 1990) with 2ν degrees of freedom and scale matrix $(2\nu\alpha^2)^{-1}I_d$, and has isotropic density

$$f_{\boldsymbol{\Omega}}(\boldsymbol{\omega}) = \frac{\Gamma(\nu + \frac{d}{2}) \alpha^d}{\Gamma(\nu) \pi^{d/2}} (1 + \alpha^2 \|\boldsymbol{\omega}\|^2)^{-(\nu+d/2)},$$

which coincides exactly with the spectral density in (8). Therefore, isotropic spectral frequencies for the \mathcal{M} model can be generated directly by sampling T and \mathbf{Z} and setting $\boldsymbol{\Omega}$ as in (9).

The \mathcal{M} correlation also admits an exact Gamma integral representation:

$$\mathcal{M}_{\nu,\alpha}(x) = \int_0^\infty \exp\left(-\frac{x^2}{2\lambda}\right) p_{\nu,\alpha}(\lambda) d\lambda, \quad (10)$$

where $\lambda \sim \text{Gamma}(\nu, 2\alpha^2)$ has density

$$p_{\nu,\alpha}(\lambda) = \frac{1}{\Gamma(\nu) (2\alpha^2)^\nu} \lambda^{\nu-1} \exp\left(-\frac{\lambda}{2\alpha^2}\right), \quad \lambda > 0.$$

The equivalence between (9) and (10) follows by the change of variable $\lambda = 2\alpha^2 T$.

This formulation leads to a simple STB sampler for the covariance model $\sigma^2 \mathcal{M}_{\nu,\alpha}$ (Emery and Lantuéjoul, 2006):

1. Set the parameters (ν, α, σ^2) and the number of spectral components L .
2. For $\ell = 1, \dots, L$:
 - (a) Sample $T_\ell \sim \text{Gamma}(\nu, 1)$;
 - (b) Sample $\mathbf{Z}_\ell \sim \mathcal{N}(\mathbf{0}, I_d)$;
 - (c) Set $\boldsymbol{\Omega}_\ell = \frac{1}{\alpha} \frac{\mathbf{Z}_\ell}{\sqrt{2T_\ell}}$;
 - (d) Sample $\Phi_\ell \sim \text{Unif}(0, 2\pi)$;
 - (e) Sample $\varepsilon_\ell \sim \text{Unif}(0, 1)$;
3. Evaluate $\tilde{Z}_L(\mathbf{s})$ at any target location $\mathbf{s} \in D$ via (6).

This exact spectral sampler yields unbiased STB realizations with the correct \mathcal{M} covariance and avoids any numerical inversion or discretization of the spectral density.

4 The Kummer–Tricomi correlation model

Ma and Bhadra (2022) introduced the \mathcal{K} family, which generalizes the \mathcal{M} class by adding a parameter that controls the tail decay of spatial correlations. This additional flexibility allows an essentially independent tuning of smoothness and tail behavior, providing a continuous bridge between the \mathcal{M} and heavier-tailed models.

For parameters $\nu > 0$ (smoothness), $\mu > 0$ (tail), and $\beta > 0$ (range or scale), the \mathcal{K} correlation function is defined as

$$\mathcal{K}_{\nu,\mu,\beta}(x) = \frac{\Gamma(\nu + \mu)}{\Gamma(\nu)} U\left(\mu, 1 - \nu, \frac{x^2}{2\beta^2}\right), \quad x \geq 0, \quad (11)$$

where $U(a, b, z)$ denotes Tricomi's confluent hypergeometric function,

$$U(a, b, z) = \frac{1}{\Gamma(a)} \int_0^\infty e^{-zt} t^{a-1} (1+t)^{b-a-1} dt.$$

For $\mu > d/2$, the model has an absolutely continuous isotropic spectral density in \mathbb{R}^d given by (Yarger and Bhadra, 2025)

$$g_R^{\mathcal{K}}(r) = \frac{\Gamma(\nu + \frac{d}{2})}{(2\pi)^{d/2} B(\mu, \nu)} \beta^d U\left(\nu + \frac{d}{2}, 1 - \mu + \frac{d}{2}, \frac{\beta^2 r^2}{2}\right), \quad r \geq 0, \quad (12)$$

where $B(\mu, \nu)$ is the Beta function. When $\mu \leq d/2$, the correlation exhibits polynomial decay, corresponding to long-range dependence, and the spectral measure is no longer absolutely continuous, so that (12) does not define a Lebesgue density.

The function $\mathcal{K}_{\nu, \mu, \beta}$ belongs to the class Φ_∞ , and is therefore positive semidefinite in any Euclidean dimension. Under an appropriate scaling, the \mathcal{M} model is recovered as a limiting case when $\mu \rightarrow \infty$; specifically,

$$\mathcal{K}_{\nu, \mu, \beta} \sqrt{2(\mu+1)}(x) \xrightarrow{\mu \rightarrow \infty} \mathcal{M}_{\nu, \beta}(x) \quad (13)$$

uniformly in x .

As shown by Ma and Bhadra (2022), $\mathcal{K}_{\nu, \mu, \beta}$ can be expressed as a continuous mixture of \mathcal{M} kernels with a random scale parameter:

$$\mathcal{K}_{\nu, \mu, \beta}(x) = \mathbb{E}_\Phi[\mathcal{M}_{\nu, \Phi}(x)], \quad \Phi^2 \sim \text{Inv-Gamma}\left(\mu, \frac{\beta^2}{2}\right), \quad (14)$$

where $\mathcal{M}_{\nu, \Phi}$ denotes the \mathcal{M} correlation (7) with smoothness ν and random scale parameter Φ .

The model also admits a stochastic representation as a Gaussian scale mixture. Let

$$X \sim \Gamma(\nu, 1), \quad Y \sim \Gamma(\mu, 1),$$

with X and Y independent, and define

$$T := \frac{X}{Y} \sim \text{BetaPrime}(\nu, \mu).$$

For $\mathbf{Z} \sim \mathcal{N}(\mathbf{0}, I_d)$ independent of (X, Y) , set

$$\boldsymbol{\Omega} = \frac{1}{\beta} \frac{\mathbf{Z}}{\sqrt{T}}.$$

Then it can be shown (see Appendix for a detailed proof) that $\boldsymbol{\Omega}$ is isotropic with density

$$f_{\boldsymbol{\Omega}}(\boldsymbol{\omega}) = \frac{\Gamma(\nu + \frac{d}{2})}{(2\pi)^{d/2} B(\mu, \nu)} \beta^d U\left(\nu + \frac{d}{2}, 1 - \mu + \frac{d}{2}, \frac{\beta^2 \|\boldsymbol{\omega}\|^2}{2}\right),$$

which coincides with the spectral density in (12). Hence, the Gaussian scale-mixture construction provides an exact sampler for isotropic spectral frequencies. The inverse-Gamma mixture form in (14) and the Gaussian scale-mixture representation above are mathematically equivalent: they are related by the transformations

$$\Phi = \frac{\beta}{\sqrt{Y}}, \quad T = \frac{X}{Y},$$

which show that the \mathcal{K} correlation can be interpreted either as a scale mixture of \mathcal{M} correlations or as a Beta-prime mixture of Gaussian components. This duality underlies the model's flexibility and provides the basis for efficient simulation.

This formulation leads to a simple STB sampler for the covariance model $\sigma^2 \mathcal{K}_{\nu, \mu, \beta}$:

1. Set the parameters $(\nu, \mu, \beta, \sigma^2)$ and the number of spectral components L .
2. For $\ell = 1, \dots, L$:
 - (a) Sample $X_\ell \sim \Gamma(\nu, 1)$ and $Y_\ell \sim \Gamma(\mu, 1)$ independently, and set $T_\ell = X_\ell/Y_\ell$;
 - (b) Sample $\mathbf{Z}_\ell \sim \mathcal{N}(\mathbf{0}, I_d)$;
 - (c) Set $\boldsymbol{\Omega}_\ell = \beta^{-1} \mathbf{Z}_\ell / \sqrt{T_\ell}$;
 - (d) Sample $\Phi_\ell \sim \text{Unif}(0, 2\pi)$;
 - (e) Sample $\varepsilon_\ell \sim \text{Unif}(0, 1)$;
3. Evaluate $\tilde{Z}_L(\mathbf{s})$ at any target location $\mathbf{s} \in D$ via (6).

This sampler is unbiased, exact, and computationally equivalent to the \mathcal{M} case, differing only by the replacement of the Gamma variable with a Beta-prime ratio.

5 The Gauss–Hypergeometric correlation model

The \mathcal{GH} class (Emery and Alegría, 2022; Bevilacqua et al., 2025a) represents one of the most general families of compactly supported correlation models currently available in spatial statistics. It provides a unified analytical framework encompassing, as special cases, the classical Wendland and Generalized Wendland models Gneiting (2002). The main appeal of this construction lies in its ability to generate covariance functions that are both *compactly supported*—leading to sparse covariance matrices—and *highly flexible* in terms of smoothness and local behavior.

For parameters $\delta > \frac{d}{2}$, $\beta > \frac{d}{2}$, $\gamma > \frac{d}{2}$, and compact-support radius $a > 0$, the \mathcal{GH} correlation model is defined as (Emery and Alegría, 2022)

$$\mathcal{GH}_{\delta, \beta, \gamma, a}(x) = \begin{cases} \frac{\Gamma(\beta - \frac{d}{2}) \Gamma(\gamma - \frac{d}{2})}{\Gamma(\beta - \delta + \gamma - \frac{d}{2}) \Gamma(\delta - \frac{d}{2})} \left(1 - \frac{x^2}{a^2}\right)^{\beta - \delta + \gamma - \frac{d}{2} - 1} {}_2F_1\left(\beta - \delta, \gamma - \delta; \beta - \delta + \gamma - \frac{d}{2}; 1 - \frac{x^2}{a^2}\right), & x \leq a, \\ 0, & x > a, \end{cases} \quad (15)$$

where sufficient conditions for the validity of the model are given by:

$$\begin{cases} \delta > \frac{d}{2} \\ 2(\beta - \delta)(\gamma - \delta) \geq \delta \\ 2(\beta + \gamma) \geq 6\delta + 1. \end{cases} \quad (16)$$

Here ${}_2F_1$ denotes Gauss's hypergeometric function, which governs the polynomial structure of the model. The isotropic *radial spectral density* associated with (15) is given by

$$g_R^{\mathcal{GH}}(r) = L(\delta, \beta, \gamma) a^d {}_1F_2\left(\delta; \beta, \gamma; -\frac{(ar)^2}{4}\right), \quad r \geq 0, \quad (17)$$

where ${}_1F_2$ is a generalized hypergeometric function and the normalizing constant is

$$L(\delta, \beta, \gamma) = \frac{\Gamma(\delta) \Gamma(\beta - \frac{d}{2}) \Gamma(\gamma - \frac{d}{2})}{2^d \pi^{d/2} \Gamma(\delta - \frac{d}{2}) \Gamma(\beta) \Gamma(\gamma)}.$$

Following the convenient parameterization of Bevilacqua et al. (2025a), we set

$$\delta = \frac{d+1}{2} + \nu, \quad \beta = \delta + \frac{\mu}{2}, \quad \gamma = \delta + \frac{\mu}{2} + l, \quad (18)$$

where $\nu > -\frac{1}{2}$ controls the differentiability at the origin, $\mu > 0$ determines the decay rate within the support, and $l \geq 0$ allows additional flexibility in the tail shape. The scale parameter $a > 0$ retains its geometric meaning as the compact-support radius.

We henceforth adopt the convenient parameterization

$$\widetilde{\mathcal{GH}}_{\nu, \mu, l, a}(x) := \mathcal{GH}_{\delta, \delta + \mu/2, \delta + \mu/2 + l, a}(x),$$

where $\delta = \frac{d+1}{2} + \nu$ as in (18).

Bevilacqua et al. (2025a) (Theorem 2) established, for $\nu > -\frac{1}{2}$ and $l > 0$, the necessary and sufficient conditions for $\widetilde{\mathcal{GH}}_{\nu, \mu, l, a}$ to be positive semidefinite on \mathbb{R}^d :

$$\begin{cases} \mu \geq \frac{d+2}{2} + \nu - l, & \text{if } 0 \leq l \leq \frac{d}{2} + \nu, \\ \mu \geq \sqrt{2\nu + l^2 + d + 1} - l, & \text{if } l > \frac{d}{2} + \nu, \end{cases} \quad (19)$$

which are equivalent to the validity conditions given in (16).

As explained in Bevilacqua et al. (2025a), while the \mathcal{GH} class is highly flexible, it suffers from identifiability issues and a simple remedy is to fix $l \geq 0$. Two particularly relevant subfamilies arise from specific choices of l :

- **Hypergeometric model:** $\mathcal{H}_{\nu, \mu, a} \equiv \widetilde{\mathcal{GH}}_{\nu, \mu, d/2 + \nu, a}$, obtained for $l = \frac{d}{2} + \nu$. This family, proposed in Bevilacqua et al. (2025a), has appealing theoretical properties; in particular, it allows one to maximize the *integral range*, with the maximum attained at $\mu = 1$. It generalizes several well-known compactly supported correlation models, such as Euclid's hat, which in turn encompasses the classical triangular, circular, and spherical models (Matheron, 1965; Gneiting, 1999).
- **Generalized Wendland model:** $\mathcal{GW}_{\nu, \mu, a} \equiv \widetilde{\mathcal{GH}}_{\nu, \mu, 1/2, a}$, obtained for $l = \frac{1}{2}$. This celebrated class was first introduced by Gneiting (2002) and has been extensively studied in spatial statistics and numerical analysis communities (Wendland, 1995; Schaback, 2011; Chernih and Hubbert, 2014; Bevilacqua et al., 2019; Bevilacqua et al., 2024).

Both the \mathcal{H} and \mathcal{GW} models, after proper rescaling of the compact support, allow one to recover the \mathcal{M} model as a limiting case. For instance Bevilacqua et al. (2022) show that:

$$\mathcal{GW}_{\nu, \mu, \beta \left(\frac{\Gamma(\mu+2\nu+1)}{\Gamma(\mu)} \right)^{\frac{1}{1+2\nu}}} (x) \xrightarrow[\mu \rightarrow \infty]{} \mathcal{M}_{\nu + \frac{1}{2}, \beta}(x), \quad (20)$$

uniformly in x .

5.1 First scale mixture representation and simulation algorithm

A remarkable property of the \mathcal{GH} family is its expression as a two-stage Beta mixture of a simpler kernel, provided that

$$\mu > 1, \quad \frac{\mu}{2} - \frac{d}{2} - \frac{1}{2} - \nu + l > 0. \quad (21)$$

Specifically, by Theorem 6 in Bevilacqua et al. (2025a),

$$\widetilde{\mathcal{GH}}_{\nu, \mu, l, a}(x) = M(\nu, \mu, l, d) \iint_{(0,1)^2} u^{\delta - \frac{d+1}{2}} (1-u)^{\frac{\mu}{2} - \frac{3}{2}} v^{\delta - \frac{1}{2} + \nu} (1-v)^{\frac{\mu}{2} - \frac{d}{2} - \frac{3}{2} - \nu + l} \mathcal{H}_{\nu, 1, a\sqrt{uv}}(x) du dv, \quad (22)$$

with

$$M(\nu, \mu, l, d) = \frac{\Gamma(\nu + \frac{\mu}{2} + \frac{1}{2}) \Gamma(\nu + \frac{\mu}{2} + \frac{1}{2} + l)}{\Gamma(\nu + 1) \Gamma(\frac{d}{2} + 2\nu + 1) \Gamma(\frac{\mu}{2} - \frac{1}{2}) \Gamma(\frac{\mu}{2} - \frac{d}{2} - \frac{1}{2} - \nu + l)}. \quad (23)$$

Writing the weights as densities of two independent Beta random variables

$$U \sim \text{Beta}\left(1 + \nu, \frac{\mu}{2} - \frac{1}{2}\right), \quad V \sim \text{Beta}\left(\frac{d}{2} + 2\nu + 1, \frac{\mu}{2} - \frac{d}{2} - \frac{1}{2} - \nu + l\right),$$

and noting that

$$M = [B(1 + \nu, \mu/2 - 1/2) B(d/2 + 2\nu + 1, \mu/2 - d/2 - 1/2 - \nu + l)]^{-1},$$

with $B(\cdot, \cdot)$ the Beta function, the above integral can be rewritten as

$$\widetilde{\mathcal{GH}}_{\nu, \mu, l, a}(x) = \mathbb{E}_{U, V} \left[\mathcal{H}_{\nu, 1, a\sqrt{UV}}(x) \right].$$

This decomposition expresses the $\widetilde{\mathcal{GH}}$ kernel as a weighted superposition of *base kernels* $\mathcal{H}_{\nu, 1, b}$ evaluated at random compact support $b = a\sqrt{UV}$, providing both theoretical insight into the structure of the $\widetilde{\mathcal{GH}}$ class and a practical route for efficient simulation.

The base kernel $\mathcal{H}_{\nu, 1, b}$ admits the conditional spectral density

$$g_R^{\widetilde{\mathcal{H}}}(r | b) = C_H(\nu, d) b^d {}_1F_2\left(\delta; \delta + \frac{1}{2}, 2\delta; -\frac{(br)^2}{4}\right), \quad r \geq 0, \quad (24)$$

where the normalization constant

$$C_H(\nu, d) = \frac{\Gamma(\frac{d+1}{2} + \nu) \Gamma(1 + \nu) \Gamma(\frac{d}{2} + 1 + 2\nu)}{2^d \pi^{d/2} \Gamma(\frac{1}{2} + \nu) \Gamma(\frac{d}{2} + 1 + \nu) \Gamma(d + 1 + 2\nu)}, \quad (25)$$

depends only on (ν, d) . Using Watson's identity (Watson, 1922, p. 147), one obtains the equivalent Bessel representation

$$g_R^{\widetilde{\mathcal{H}}}(r | b) = C_H(\nu, d) b^d \Gamma^2(\delta + \frac{1}{2}) \left(\frac{br}{4}\right)^{1-2\delta} J_{\delta - \frac{1}{2}}^2\left(\frac{br}{2}\right), \quad (26)$$

which highlights the oscillatory yet non-negative nature of the spectral density. The factor $C_H(\nu, d)$ controls the overall normalization and plays a key role in the universal sampling mechanism described below.

Let $T := bR$. It can be shown (see Appendix) that the distribution of T does not depend on b . Its density is

$$\begin{aligned} f_T(t) &= |\mathbb{S}^{d-1}| t^{d-1} C_H(\nu, d) {}_1F_2\left(\delta; \delta + \frac{1}{2}, 2\delta; -\frac{t^2}{4}\right) \\ &= |\mathbb{S}^{d-1}| t^{d-1} C_H(\nu, d) \Gamma^2(\delta + \frac{1}{2}) \left(\frac{t}{4}\right)^{1-2\delta} J_{\delta - \frac{1}{2}}^2\left(\frac{t}{2}\right), \quad t \geq 0. \end{aligned} \quad (27)$$

This *universal* auxiliary distribution encapsulates the spectral behavior shared by all $\widetilde{\mathcal{GH}}$ models in the parametric region defined by (21), independently of (μ, l, a) . It allows the sampling of the spectral radius to be decomposed into two independent components: (1) a universal draw of T , and (2) a local rescaling via $b = a\sqrt{UV}$.

Combining the mixture representation (22) with the auxiliary variable (27) leads to a simple and exact STB algorithm for the covariance model $\sigma^2 \widetilde{\mathcal{GH}}_{\nu, \mu, l, a}$:

1. Set the parameters $(\nu, \mu, l, a, \sigma^2)$ and the number of spectral components L .
2. For $\ell = 1, \dots, L$:
 - (a) Sample $U_\ell \sim \text{Beta}(1+\nu, \frac{\mu}{2} - \frac{1}{2})$ and $V_\ell \sim \text{Beta}(\frac{d}{2} + 2\nu + 1, \frac{\mu}{2} - \frac{d}{2} - \frac{1}{2} - \nu + l)$ independently;
 - (b) Set $b_\ell = a\sqrt{U_\ell V_\ell}$;
 - (c) Sample T_ℓ from the universal distribution f_T defined in (27);
 - (d) Set the spectral radius as $R_\ell = T_\ell/b_\ell$;
 - (e) Sample $\Theta_\ell \sim \text{Unif}(\mathbb{S}^{d-1})$ and define $\Omega_\ell = R_\ell \Theta_\ell$;
 - (f) Sample $\Phi_\ell \sim \text{Unif}(0, 2\pi)$;
 - (g) Sample $\varepsilon_\ell \sim \text{Unif}(0, 1)$;
3. Evaluate $\tilde{Z}_L(\mathbf{s})$ at any target location using (6).

The STB algorithm thus requires sampling from the universal auxiliary variable T . Direct sampling from this distribution is challenging due to its oscillatory nature and the absence of a closed-form inverse cumulative distribution function. To address this, we employ an adaptive rejection sampling scheme (Devroye, 1986) based on a mixture proposal. The support $(0, \infty)$ is partitioned at a threshold t_0 into *body* and *tail* regions, with respective proposal densities:

$$g_1(t) = \frac{dt^{d-1}}{t_0^d}, \quad 0 \leq t \leq t_0, \quad (28)$$

$$g_2(t) = \frac{\alpha t_0^\alpha}{t^{\alpha+1}}, \quad t > t_0, \quad (29)$$

where $\alpha = 2\nu + 2$ matches the tail decay of f_T . Both proposals allow exact sampling: $T = t_0 U^{1/d}$ for g_1 and $T = t_0 (1-U)^{-1/\alpha}$ for g_2 , with $U \sim \text{Unif}(0, 1)$. The threshold t_0 is selected by minimizing the sum of the envelope constants:

$$t_0^* = \arg \min_{t_0 > 0} \{M_1(t_0) + M_2(t_0)\}, \quad (30)$$

where M_i are chosen such that $f_T(t) \leq M_i g_i(t)$ in each region. At the optimum, the envelope constants are approximately balanced ($M_1 \approx M_2$), leading to acceptance rates of 50–60% across typical parameter ranges. The mixture weights are set as $w_1 = M_1/(M_1 + M_2)$ and $w_2 = 1 - w_1$. This adaptive approach substantially outperforms fixed heuristic thresholds (which typically yield $\approx 15\%$ acceptance) and requires no numerical integration. The sampler is exact in distribution and scales efficiently to large sample sizes.

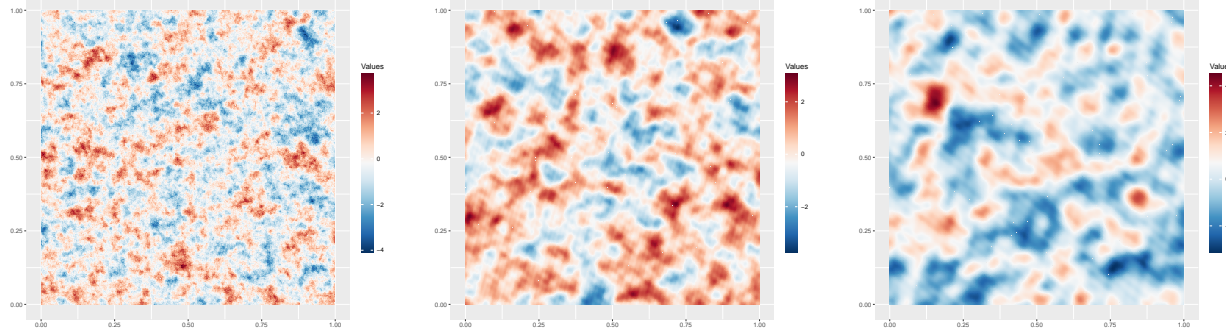


Figure 1: Simulated Gaussian RFs on 1,000,000 points uniformly distributed on $[0, 1]^2$ using the correlation model $\mathcal{GW}_{\nu,7,0.2} \equiv \widetilde{\mathcal{GH}}_{\nu,7,1/2,0.2}$ with increasing smoothness levels $\nu = 0, 1, 2$ (from left to right).

As an example, Figure 1 illustrates three realizations of a Gaussian RF on 1,000,000 points uniformly distributed on $[0, 1]^2$, obtained with the proposed algorithm ($L = 1,000$) using the correlation model $\mathcal{GW}_{\nu,7,0.2} \equiv \widetilde{\mathcal{GH}}_{\nu,7,1/2,0.2}$ with increasing smoothness levels $\nu = 0, 1, 2$ (from left to right).

The Beta variables in Step 2 are well defined under conditions (21). These conditions ensure non-degenerate mixtures and hence simulability. They are slightly more restrictive than the mere positive-definiteness conditions in (19), implying that all simulatable models are valid, although not all valid models admit a mixture-based sampler.

In the boundary cases, i.e., $\mu \rightarrow 1$ and/or $\frac{\mu}{2} - \frac{d}{2} - \frac{1}{2} - \nu + l \rightarrow 0$, the corresponding Beta distributions collapse to degenerate point masses and the mixture representation (22) ceases to hold in its integral form. Nevertheless, these limiting situations correspond to meaningful, well-defined correlation models that remain members of the \mathcal{GH} class.

The interval where the model is valid but not simulatable corresponds to parameter combinations that violate (21) without breaching (19). As an illustration, Figure 2 displays the (μ, ν) regions of validity and simulability for $d = 2$: the left panel refers to the \mathcal{GW} model ($l = 0.5$), while the right panel corresponds to the \mathcal{H} model ($l = d/2 + \nu$). It is apparent that the simulability region (in green) is strictly contained within the validity region, highlighting the existence of parameter configurations that are valid yet non-simulatable with our approach. Notably, for the \mathcal{H} model, the non-simulatable region (in yellow) is larger than that of the \mathcal{GW} model, indicating a narrower range of parameters for which the Beta-mixture sampler remains feasible.

5.2 Second scale mixture representation and simulation algorithm

To overcome the limitations of the Beta-mixture representation in the non-simulatable region, we introduce an alternative and more general spectral representation, derived from Gasper's decomposition of the hypergeometric kernel. Specifically, using the original parameterization (δ, β, γ) , the radial spectral density (17) of the \mathcal{GH} kernel can be rewritten as (Gasper, 1975, Eq. 3.1)

$$g_R^{\mathcal{GH}}(r) = L(\delta, \beta, \gamma) a^d \Gamma^2(\eta + 1) \left(\frac{ar}{4}\right)^{-2\eta} \sum_{n=0}^{\infty} C(n, \delta, \beta, \gamma) \frac{(2n + 2\eta)(2\eta + 1)_n}{(n + 2\eta)n!} J_{\eta+n}^2 \left(\frac{ar}{2}\right),$$

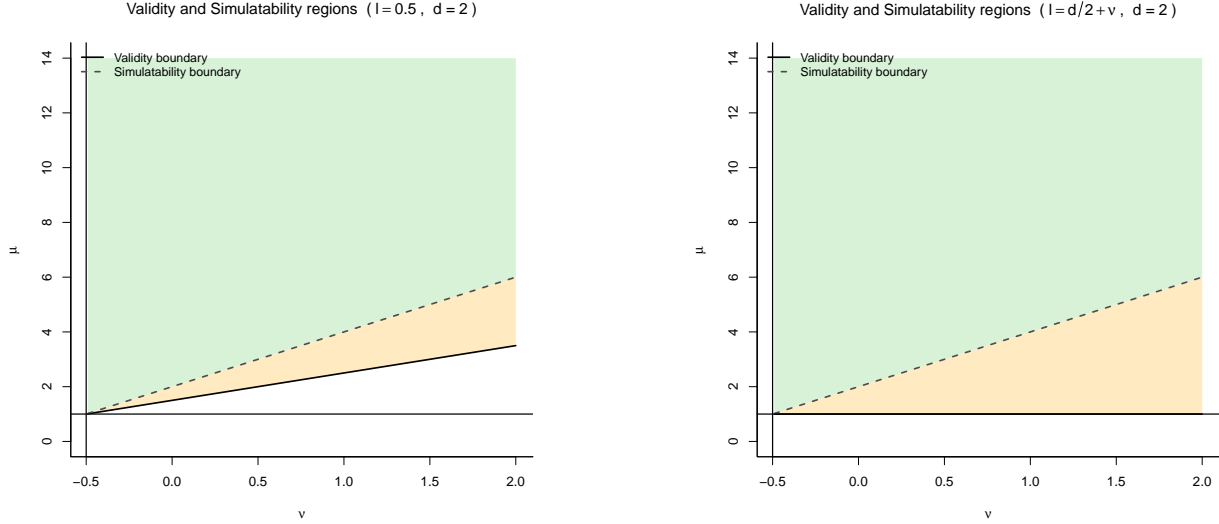


Figure 2: Validity (yellow and green) and simulability (green) regions in the (ν, μ) plane for $d = 2$. The left panel corresponds to the \mathcal{GW} model ($l = 0.5$), while the right panel refers to the \mathcal{H} model ($l = d/2 + \nu$). The solid black line denotes the validity boundary, whereas the dashed black line marks the simulability limit of the Beta-mixture sampler.

where $(\cdot)_n$ denotes the Pochhammer symbol, $\eta = \frac{1}{2}(\beta + \gamma - \delta - \frac{3}{2})$, and

$$C(n, \delta, \beta, \gamma) = {}_4F_3\left(-n, n + 2\eta, \eta + 1, \delta; \eta + \frac{1}{2}, \beta, \gamma; 1\right),$$

which can be evaluated numerically without difficulty, as the hypergeometric function ${}_4F_3$ is a terminating series. Its explicit series representation reads

$$C(n, \delta, \beta, \gamma) = \sum_{k=0}^n \frac{(-n)_k (n + 2\eta)_k (\eta + 1)_k (\delta)_k}{(\eta + \frac{1}{2})_k (\beta)_k (\gamma)_k k!},$$

and it can be computed recursively using the update rule

$$t_{k+1} = t_k \frac{(-n + k) (n + 2\eta + k) (\eta + 1 + k) (\delta + k)}{(\eta + \frac{1}{2} + k) (\beta + k) (\gamma + k) (k + 1)}, \quad t_0 = 1, \quad C(n, \delta, \beta, \gamma) = \sum_{k=0}^n t_k.$$

Defining

$$\begin{aligned} g_R^{(n)}(r \mid d/2 + \nu, a) &= C_H(\nu, d, n) a^{d+2n} r^{2n} {}_1F_2\left(\frac{d+1}{2} + \nu; \frac{d}{2} + 1 + \nu, d + 1 + 2\nu; -\frac{(ar)^2}{4}\right) \\ &= C_H(\nu, d, n) a^{d+2n} r^{2n} \Gamma^2\left(\frac{d}{2} + 1 + \nu\right) \left(\frac{ar}{4}\right)^{-d-2\nu} J_{\frac{d}{2}+\nu}^2\left(\frac{ar}{2}\right), \end{aligned} \quad (31)$$

with

$$C_H(\nu, d, n) = \frac{\Gamma(\frac{d}{2}) \Gamma(\frac{d+1}{2} + \nu) \Gamma(1 + \nu - n) \Gamma(\frac{d}{2} + 1 + 2\nu - n)}{2^{d+2n} \pi^{d/2} \Gamma(\frac{d}{2} + n) \Gamma(\frac{1}{2} + \nu - n) \Gamma(\frac{d}{2} + 1 + \nu) \Gamma(d + 1 + 2\nu)},$$

we obtain

$$g_R^{\mathcal{GH}}(r) = \sum_{n=0}^{\infty} w_n(\delta, \beta, \gamma) g_R^{(n)}(r \mid \eta + n, a), \quad (32)$$

where

$$w_n(\delta, \beta, \gamma) = \frac{L(\delta, \beta, \gamma) \Gamma^2(\eta + 1)}{2^{4n} \Gamma^2(\eta + n + 1)} \frac{C(n, \delta, \beta, \gamma)}{C_H(\eta + n - \frac{d}{2}, d, n)} \frac{(2n + 2\eta)(2\eta + 1)_n}{(n + 2\eta)n!}. \quad (33)$$

On the one hand, Emery et al. (2025, Theorem 2) proved that $\omega \mapsto g_R^{(n)}(\|\omega\| \mid \eta + n, a)$ is the spectral density of an isotropic correlation function in \mathbb{R}^d , hence a probability density function on \mathbb{R}^d . Let $\Omega \in \mathbb{R}^d$ be a frequency vector with density $g_R^{(n)}(\|\omega\| \mid \eta + n, a)$, $R = \|\Omega\|$, and $T := aR$. It can be shown (see Appendix) that the distribution of T does not depend on a , and that its density is

$$f_T^{(n)}(t) = |\mathbb{S}^{d-1}| \frac{C_H(\eta + n - \frac{d}{2}, d, n) 4^{2\eta+2n} \Gamma^2(1 + \eta + n)}{t^{1-d+2\eta}} J_{\eta+n}^2\left(\frac{t}{2}\right), \quad t > 0. \quad (34)$$

Because $t \mapsto J_{\eta+n}(t)$ behaves like $t^{\eta+n}$ for small t and like a cosine function multiplied by $t^{-1/2}$ for large t , this density remains bounded on $(0, \infty)$.

On the other hand, Cho et al. (2020, Lemma 3.1) proved that, under conditions (16), $C(n, \delta, \beta, \gamma)$ is non-negative. Since both $g_R^{\mathcal{GH}}(\|\cdot\|)$ and $g_R^{(n)}(\|\cdot\| \mid \eta + n, a)$ integrate to one on \mathbb{R}^d , it follows that the weights $w_n(\delta, \beta, \gamma)$ are non-negative and sum to 1. As conditions (16) coincide with those in (19), the Gasper–mixture representation is more general than the Beta–mixture formulation and covers the entire region of validity of the $\widehat{\mathcal{GH}}$ model.

Based on this decomposition, the following exact STB algorithm can be used to generate realizations in the region of the covariance model $\sigma^2 \widehat{\mathcal{GH}}_{\nu, \mu, l, a}$ that is non-simulatable with the Beta–mixture sampler:

1. Set the parameters $(\nu, \mu, l, a, \sigma^2)$ and the number of spectral components L .
2. Set $\delta = \frac{d+1}{2} + \nu$, $\beta = \delta + \frac{\mu}{2}$, and $\gamma = \delta + \frac{\mu}{2} + l$.
3. For $\ell = 1, \dots, L$:
 - (a) Sample $U_\ell \sim \text{Unif}(0, 1)$;
 - (b) Compute $w_n(\delta, \beta, \gamma)$ as in (33);
 - (c) Find the smallest integer N_ℓ such that $\sum_{n=0}^{N_\ell} w_n(\delta, \beta, \gamma) > U_\ell$;
 - (d) Sample T_ℓ from the distribution $f_T^{(N_\ell)}$ defined in (34);
 - (e) Set the spectral radius as $R_\ell = T_\ell/a$;
 - (f) Sample $\Theta_\ell \sim \text{Unif}(\mathbb{S}^{d-1})$ and define $\Omega_\ell = R_\ell \Theta_\ell$;
 - (g) Sample $\Phi_\ell \sim \text{Unif}(0, 2\pi)$;
 - (h) Sample $\varepsilon_\ell \sim \text{Unif}(0, 1)$;
4. Evaluate $\tilde{Z}_L(\mathbf{s})$ at any target location \mathbf{s} using (6).

As in the previous section, STB simulation requires sampling from an auxiliary radial variable T , whose density $f_T^{(n)}$ is given in (34). Although $f_T^{(n)}$ involves oscillatory Bessel components similar to those of f_T in (27), it remains strictly non-negative and bounded on $(0, \infty)$. Therefore, the same adaptive rejection strategy as before is employed, based on a two-component body-tail proposal:

$$g_1(t) \propto t^{d-1}, \quad g_2(t) \propto t^{-\alpha-1}, \quad \alpha = 2\eta + 1 - d,$$

with a data-driven threshold t_0 selected to balance the corresponding envelope constants. This construction ensures stable and efficient acceptance rates, with typical values between 40% and 55% across a wide range of dimensions and parameters.

Each frequency component is then generated by first sampling the discrete index n according to the non-negative weights $w_n(\delta, \beta, \gamma)$, then drawing the corresponding auxiliary variable T from the density $f_T^{(n)}$, and finally rescaling by the compact-support parameter a to obtain the spectral radius $R = T/a$.

6 Numerical experiments

Throughout this section, we consider a Gaussian RF $\{Z(\mathbf{s}) : \mathbf{s} \in D \subset \mathbb{R}^2\}$, with mean $\mathbb{E}[Z(\mathbf{s})] = 0$ and variance $\mathbb{V}[Z(\mathbf{s})] = \sigma^2 = 1$. To assess the accuracy of the proposed simulation algorithms, we generate 1,000 independent realizations of a Gaussian RF with different covariance functions over 5,000 spatial locations uniformly distributed on $[0, 1]^2$. All simulations were performed using the proposed algorithms with $L = 1,000$ spectral components.

We first focus on the Generalized Wendland model $\mathcal{GW}_{\nu, \mu, a} \equiv \widetilde{\mathcal{GH}}_{\nu, \mu, 1/2, a}$. The parameters are chosen to obtain a diverse set of covariance structures. Since the smoothness parameter ν controls the mean-square differentiability of the field, we set $\nu = 0$ for a non-differentiable Gaussian RF and $\nu = 1$ for smooth realizations. We also consider two different compact support parameters, $a = 0.1$ and $a = 0.5$, which determine the finite correlation range.

The shape parameter μ affects the behavior of the covariance function, particularly at small distances, and determines which simulation algorithm is applicable. We take $\mu = 6, 7$ to use the first algorithm based on the Beta-mixture representation (Section 5.1), and $\mu = 2, 3$ to use the second algorithm based on the Gasper-mixture representation (Section 5.2).

This setup yields eight different scenarios, summarized in Tables 1 and 2. As a diagnostic of the simulation accuracy, we follow Emery et al. (2016); Cuevas et al. (2020); Arroyo and Emery (2021) and compute the omnidirectional empirical semivariogram for each realization.

For each parameter configuration, 1,000 semivariograms are computed from the corresponding realizations. On average over the realizations, the empirical semivariograms closely follow their theoretical counterparts, indicating that the simulation algorithms behave as expected and that the underlying numerical procedures are stable and accurate for both algorithms. The results are displayed in Figures 3 and 4, where we also report empirical semivariograms obtained from realizations generated with the standard Cholesky method.

The same experimental design is used for the Kummer-Tricomi model $\mathcal{K}_{\nu, \mu, \beta}$. As the smoothness parameter ν controls the mean-square differentiability of the RF, we consider $\nu = 0.5$ for a non-differentiable Gaussian RF and $\nu = 1.5$ to obtain smooth realizations. We also consider two different scale parameters, $\beta = 0.1$ and $\beta = 0.5$, which are related to the correlation range. The tail parameter μ governs the behavior of the correlation function at large distances and can give rise to

either short-range or long-range dependence. Here, we take $\mu = 0.25$ (long-range dependence) and $\mu = 1.5$ (short-range dependence). This setup yields six different scenarios, summarized in Table 3.

As in the Generalized Wendland case, the empirical semivariograms of the realizations closely match their theoretical counterparts, showing that the simulation algorithm performs as expected and that the numerical procedures are stable and accurate for this covariance model under both short- and long-range dependence. The results are reported in Figure 5.

Table 1: Parameters of the $\mathcal{GW}_{\nu,\mu,a}$ (Generalized Wendland correlation model) used in the simulation study. The parameters are chosen such that $\mu/2 - 1 - \nu > 0$, corresponding to the Beta-mixture algorithm (Section 5.1).

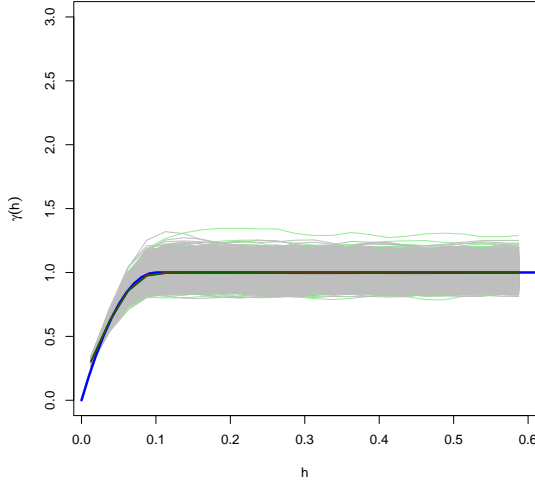
Scenario	Smoothness (ν)	Compact support (a)	Shape (μ)	Algorithm
1	0	0.1	6	Beta-mixture
2	1	0.1	7	Beta-mixture
3	0	0.5	6	Beta-mixture
4	1	0.5	7	Beta-mixture

Table 2: Parameters of the $\mathcal{GW}_{\nu,\mu,a}$ (Generalized Wendland correlation model) used in the simulation study. The parameters are chosen such that $\mu/2 - 1 - \nu < 0$, corresponding to the Gasper-mixture algorithm (Section 5.2).

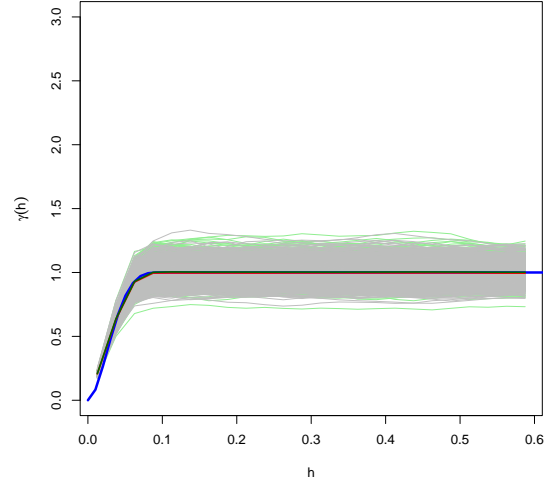
Scenario	Smoothness (ν)	Compact support (a)	Shape (μ)	Algorithm
5	0	0.1	2	Gasper-mixture
6	1	0.1	3	Gasper-mixture
7	0	0.5	2	Gasper-mixture
8	1	0.5	3	Gasper-mixture

Table 3: Parameters of the $\mathcal{K}_{\nu,\mu,\beta}$ (Kummer–Tricomi) correlation model used in the simulation study. The tail parameter μ is chosen to explore short-range dependence (Scenarios 9, 11, 13) and long-range dependence (Scenarios 10, 12, 14), while the scale parameter β is chosen such that $\mathcal{K}_{\nu,\mu,\beta}(0.1) = 0.90$ (Scenarios 9–11) or $\mathcal{K}_{\nu,\mu,\beta}(0.5) = 0.90$ (Scenarios 12–14).

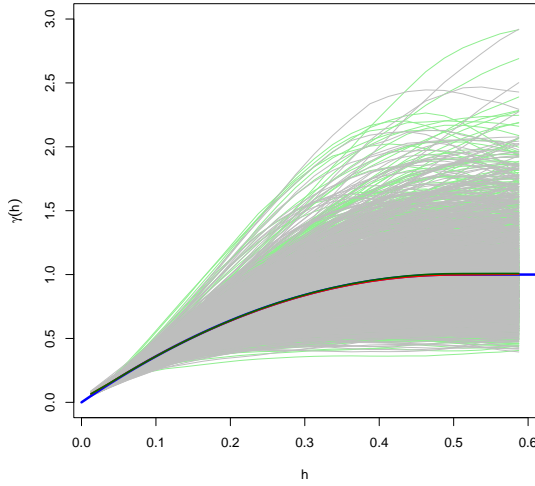
Scenario	Smoothness (ν)	Scale (β)	Tail (μ)
9	0.5	0.101	3.5
10	0.5	0.013	0.25
11	1.5	0.059	3.5
12	1.5	0.032	0.25
13	1.5	0.293	3.5
14	0.5	0.064	0.25



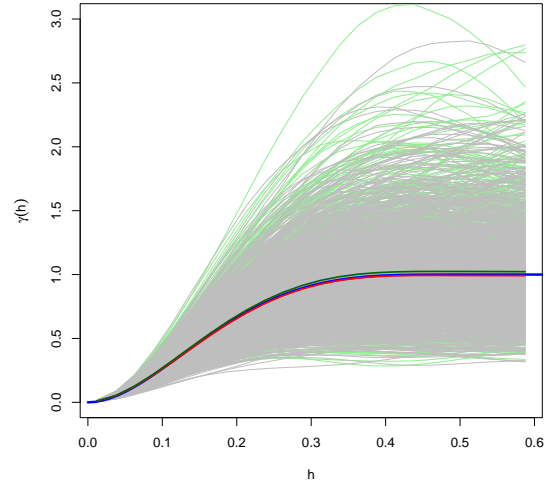
(a) Scenario 1



(b) Scenario 2

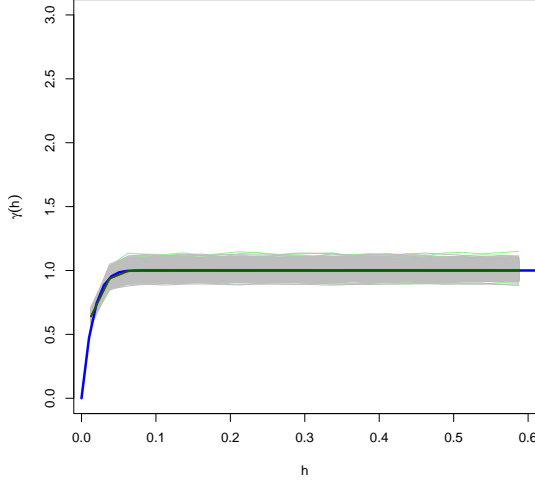


(c) Scenario 3

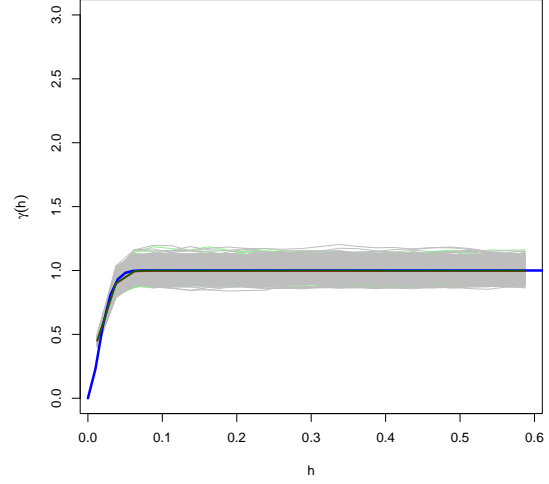


(d) Scenario 4

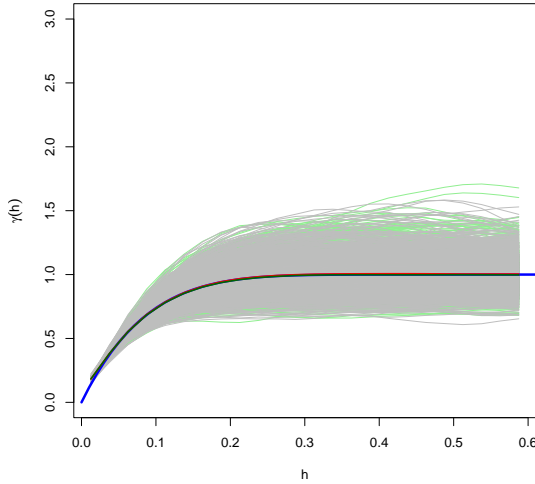
Figure 3: Empirical semivariograms from 1,000 realizations of a Gaussian RF under different parameter configurations of the $\mathcal{GW}_{\nu,\mu,a}$ correlation function (Generalized Wendland; see Table 1), generated using the Beta-mixture algorithm. Gray lines show the empirical semivariograms for individual realizations, red lines their empirical mean over the 1,000 realizations, and blue lines the corresponding theoretical semivariograms. Green lines show empirical semivariograms computed from realizations obtained via the Cholesky method.



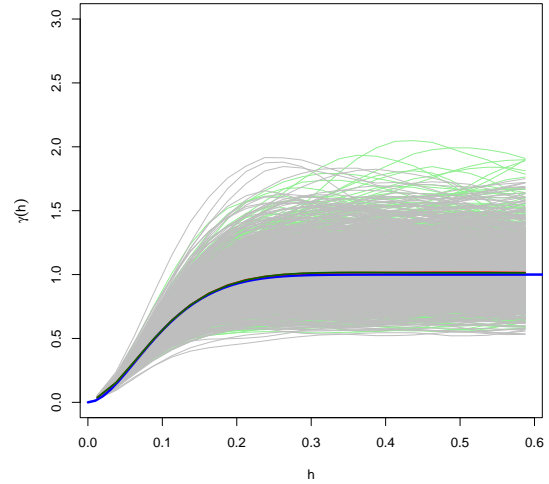
(a) Scenario 5



(b) Scenario 6



(c) Scenario 7



(d) Scenario 8

Figure 4: Empirical semivariograms from 1,000 realizations of a Gaussian RF under different parameter configurations of the $\mathcal{GW}_{\nu,\mu,a}$ correlation function (Generalized Wendland; see Table 2), generated using the Gasper-mixture algorithm. Gray lines show the empirical semivariograms for individual realizations, red lines their empirical mean over the 1,000 realizations, and blue lines the corresponding theoretical semivariograms. Green lines show empirical semivariograms computed from realizations obtained via the Cholesky method.

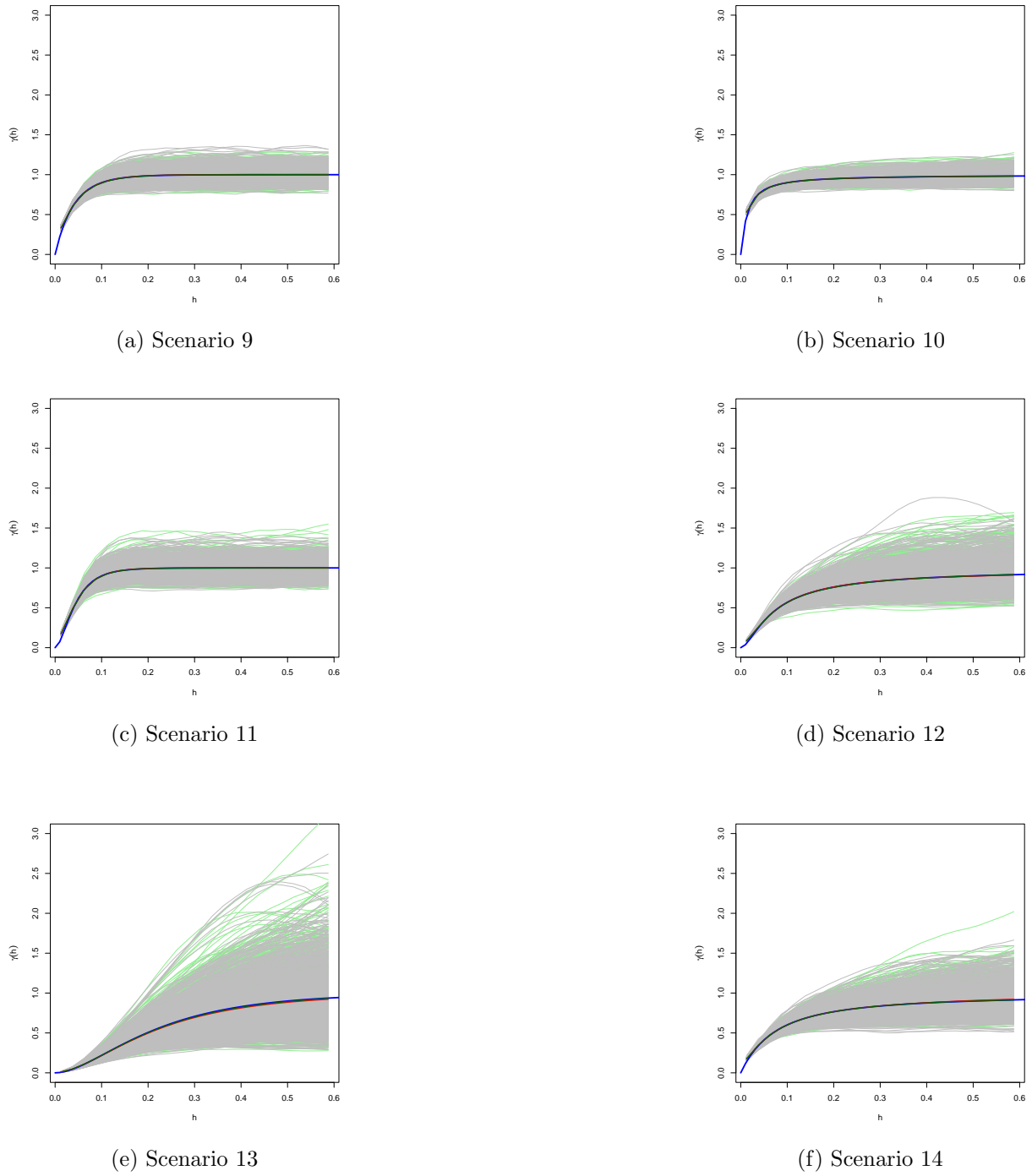


Figure 5: Empirical semivariograms from 1,000 realizations of a Gaussian RF under different parameter configurations of the $\mathcal{K}_{\nu,\mu,\beta}$ correlation function (see Table 3) using the proposed algorithm. Gray lines show the empirical semivariograms for individual realizations, red lines their empirical mean over the 1,000 realizations, and blue lines the corresponding theoretical semivariograms. Green lines show empirical semivariograms computed from realizations obtained via the Cholesky method.

7 Analysis of climate data using weighted composite likelihood

7.1 Composite likelihood, variability estimation, and parametric bootstrap

Composite likelihood (CL) estimation methods (B. Lindsay, 1988; Varin et al., 2011) provide a flexible and computationally convenient alternative to full likelihood when the joint density is analytically intractable or too expensive to evaluate. In spatial statistics, composite likelihoods based on low-dimensional margins, and in particular on *pairs*, are especially attractive for large datasets and complex dependence structures. Some successful applications can be found in Patrick J. Heagerty and Lele (1998); Bevilacqua et al. (2020); Morales-Navarrete et al. (2024), among others.

Let $\mathbf{Y} = (Y(\mathbf{s}_1), \dots, Y(\mathbf{s}_n))^\top$ denote the vector of observations at locations $\{\mathbf{s}_1, \dots, \mathbf{s}_n\} \subset D \subset \mathbb{R}^d$, with joint distribution indexed by a parameter vector $\boldsymbol{\theta} \in \Theta \subset \mathbb{R}^p$. For $1 \leq i < j \leq n$, let $\mathbf{Y}_{ij} = (Y(\mathbf{s}_i), Y(\mathbf{s}_j))^\top$ and denote by $f_{\mathbf{Y}_{ij}}(\cdot; \boldsymbol{\theta})$ the associated bivariate density. The *weighted composite likelihood based on pairs* (WCLP) is defined as

$$wclp(\boldsymbol{\theta}) = \sum_{i=1}^n \sum_{j \neq i} w_{ij} l_{ij}(\boldsymbol{\theta}), \quad l_{ij}(\boldsymbol{\theta}) = \log f_{\mathbf{Y}_{ij}}(y_{ij}; \boldsymbol{\theta}), \quad (35)$$

and the corresponding estimator is

$$\hat{\boldsymbol{\theta}} = \arg \max_{\boldsymbol{\theta} \in \Theta} wclp(\boldsymbol{\theta}).$$

The weights w_{ij} in (35) play a key role in reducing computational costs and improving efficiency (Bai et al., 2014; Bevilacqua and Gaetan, 2015; Feng et al., 2014; Patrick J. Heagerty and Lele, 1998; Varin and Vidoni, 2005). Following Caamaño-Carrillo et al. (2024), a computationally and statistically efficient strategy is to restrict w_{ij} to nearest neighbors. Specifically, let $N_m(\mathbf{s}_j)$ denote the set of m nearest neighbors of location $\mathbf{s}_j \in D$. The weight function is then defined as

$$w_{ij}(m) = \begin{cases} 1, & \mathbf{s}_i \in N_m(\mathbf{s}_j), \\ 0, & \text{otherwise,} \end{cases} \quad (36)$$

for $i, j = 1, \dots, n$, $i \neq j$. This choice is computationally convenient because kd-tree algorithms (Arya et al., 1998; Elseberg et al., 2012) allow an efficient construction of nearest neighbor sets. In particular, with this construction, the cost of evaluating $wclp(\boldsymbol{\theta})$ and its derivatives grows essentially linearly with n and remains manageable even for very large datasets.

A major challenge in composite likelihood inference is the assessment of estimator variability and the construction of hypothesis tests. Under increasing-domain asymptotics and suitable regularity and mixing conditions, the WCLP estimator $\hat{\boldsymbol{\theta}}$ is consistent and asymptotically normal, with covariance matrix given by the inverse *Godambe information* (Bevilacqua and Gaetan, 2015)

$$G^{-1}(\boldsymbol{\theta}) = H(\boldsymbol{\theta})^{-1} J(\boldsymbol{\theta}) H(\boldsymbol{\theta})^{-1},$$

where

$$H(\boldsymbol{\theta}) = \mathbb{E}[-\nabla^2 wclp(\boldsymbol{\theta})], \quad J(\boldsymbol{\theta}) = \text{Var}[\nabla wclp(\boldsymbol{\theta})].$$

The matrix $H(\boldsymbol{\theta})$ is the *sensitivity* and $J(\boldsymbol{\theta})$ the *variability* of the composite score. In practice, $H(\boldsymbol{\theta})$ can be approximated by the observed Hessian matrix, but estimating $J(\boldsymbol{\theta})$ is considerably

more difficult from a computational viewpoint, as it involves the covariance structure of composite scores.

Several approaches have been proposed to approximate $J(\boldsymbol{\theta})$, including subsampling and block-based methods (Carlstein, 1986; Politis and Romano, 1994), where one computes the covariance of the composite score over spatial blocks or windows and aggregates the results (e.g. Patrick J. Heagerty and Lele, 1998; Bevilacqua and Gaetan, 2015). However, these procedures typically depend on tuning parameters such as the block size and shape, may be sensitive to their choice, and can be computationally demanding for large datasets. Moreover, the standard increasing-domain asymptotic framework does not cover fixed-domain settings, for which asymptotic results for composite likelihood estimators are more scarce and often not directly applicable (Bachoc et al., 2019).

In this context, parametric bootstrap emerges as a powerful and conceptually simple tool for variance estimation and hypothesis testing. Starting from a fitted model $\hat{\boldsymbol{\theta}}$, one simulates B independent datasets from the model, re-estimates the parameters on each dataset by maximizing (35), and uses the empirical covariance of the bootstrap estimates to approximate $G^{-1}(\boldsymbol{\theta})$. This approach automatically accounts for the complex dependence structure encoded in the composite likelihood and avoids explicit evaluation of $J(\boldsymbol{\theta})$.

Other quantities of interest can then be estimated, such as the composite likelihood Akaike information criterion (CLAIC) (Varin and Vidoni, 2005),

$$\text{CLAIC} = -2 wclp(\boldsymbol{\theta}) + 2 \text{tr}(H(\boldsymbol{\theta}) G(\boldsymbol{\theta})^{-1}), \quad (37)$$

by plugging-in a bootstrap estimate of $G^{-1}(\boldsymbol{\theta})$, as well as composite-likelihood-based test statistics (see Varin et al. (2011) and references therein).

The main drawback of the parametric bootstrap in spatial applications is computational: each bootstrap replicate requires the simulation of a large (possibly non-Gaussian) random field under the fitted model. When the number of locations n is large, classical simulation methods based on Cholesky factorization, circulant embedding or Markov approximations become prohibitively expensive or require restrictive assumptions on the sampling design. The STB algorithms developed in this paper for the \mathcal{M} , \mathcal{K} , and \mathcal{GH} families make parametric bootstrap feasible for large spatial datasets by enabling fast simulation of (non-)Gaussian random fields with flexible correlation structures. In what follows, we illustrate this strategy by analyzing a large climate dataset using WCLP, parametric bootstrap, and the proposed STB samplers.

7.2 Data description and model specification

We consider mean May temperature data from the WorldClim 2.1 database (www.worldclim.org), a global source of high-resolution gridded climate data for the period 1970–2000, which can be downloaded using the R package `geodata` (Hijmans et al., 2023). In this application, we focus on $n = 132,667$ locations covering the Republic of Ireland, extracted from the original 30" (approximately 1 km) grid. All coordinates are expressed in a suitable UTM projection. The data are randomly split into a training set (85% of locations) used for parameter estimation, and a validation set (15%) used for evaluating predictive performance.

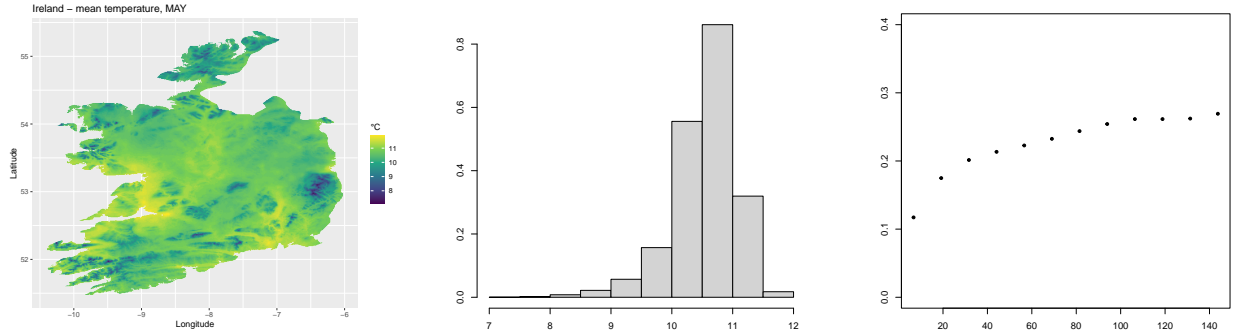


Figure 6: From left to right: spatial map, normalized histogram, and empirical semivariogram of mean May temperature in Ireland for the period 1970–2000.

A preliminary exploratory analysis (see Figure 6) reveals clear departures from Gaussianity. In particular, the histogram suggests that the Gaussian assumption is inappropriate, indicating that an RF with asymmetric and heavy-tailed marginal distributions may be more suitable. By contrast, weak stationarity appears to be a reasonable assumption, and the empirical semivariogram shows a slow decay of dependence with distance. To account for these features, we adopt an additive modeling strategy of the form

$$Y(\mathbf{s}_i) = \mu + \sigma X(\mathbf{s}_i), \quad i = 1, \dots, n, \quad (38)$$

where μ is a location parameter, $\sigma > 0$ is a scale parameter, and $\{X(\mathbf{s}) : \mathbf{s} \in D\}$ is a second-order stationary RF. We consider two specifications for X :

1. **Gaussian RF:**

$$X(\mathbf{s}) = Z(\mathbf{s}),$$

where Z is a zero-mean, unit-variance Gaussian RF.

2. **Sinh–arcsinh RF:**

$$X(\mathbf{s}) = \sinh\left(\frac{\sinh^{-1}\{Z(\mathbf{s})\} + \eta}{\chi}\right),$$

where $\eta \in \mathbb{R}$ controls skewness and $\chi > 0$ controls tail heaviness. For $(\eta, \chi) = (0, 1)$ the model reduces to the Gaussian case, whereas $\eta \neq 0$ and/or $\chi \neq 1$ produce asymmetric and/or heavy-tailed marginals (see Blasi et al. (2022) for more details on Sinh–arcsinh RFs).

In both cases, the underlying Gaussian random field Z has an isotropic correlation function belonging to one of the following families:

- (a) **Matérn model** $\mathcal{M}_{\nu, \beta}$, with smoothness parameter $\nu > 0$ and spatial scale parameter $\beta > 0$, as in (7).
- (b) **Kummer–Matérn model** $\mathcal{KM}_{\nu, \mu, \beta}$, defined as the reparameterized Kummer–Tricomi model

$$\mathcal{KM}_{\nu, \mu, \beta}(x) := \mathcal{K}_{\nu, \mu, \beta} \sqrt{2(\mu+1)}(x),$$

see (13). The parameter $\nu > 0$ again controls smoothness, $\mu > 0$ is a tail parameter, and $\beta > 0$ is a spatial scale parameter; small values of μ allow for pronounced long-range dependence.

(c) **Wendland–Matérn model** $\mathcal{WM}_{\nu,\mu,\beta}$, defined as the reparameterized Generalized Wendland model

$$\mathcal{WM}_{\nu,\mu,\beta}(x) := \mathcal{GW}_{\nu,\mu,\beta\left(\frac{\Gamma(\mu+2\nu+1)}{\Gamma(\mu)}\right)^{\frac{1}{1+2\nu}}}(x),$$

see (20). Here $\nu > -\frac{1}{2}$ is a smoothness parameter, $\mu > 0$ a shape parameter, and $\beta > 0$ affects the compact support, whose radius is $\beta\left(\frac{\Gamma(\mu+2\nu+1)}{\Gamma(\mu)}\right)^{\frac{1}{1+2\nu}}$.

Under the rescalings in (20) and (13), both $\mathcal{WM}_{\nu,\mu,\beta}$ and $\mathcal{KM}_{\nu,\mu,\beta}$ converge to a \mathcal{WM} correlation as $\mu \rightarrow \infty$. In our application, we keep μ fixed in order to represent two extreme departures from the \mathcal{WM} benchmark: we take $\mu = 3$ for $\mathcal{WM}_{\nu,\mu,\beta}$, yielding a Matérn–like model with compact support, and $\mu = 1.5$ for $\mathcal{KM}_{\nu,\mu,\beta}$, producing a Matérn–like model with heavier decay of the \mathcal{WM} model. In addition, a preliminary estimation step suggests that the smoothness parameter of the \mathcal{WM} model is close to 0.5. We therefore compare the correlation models $\mathcal{M}_{0.5,\beta}$, $\mathcal{WM}_{0.3,\beta}$ and $\mathcal{KM}_{0.5,1.5,\beta}$.

Note that the properties of the correlation functions (a), (b), and (c) are inherited by the correlation function of the Sinh–arcsinh RF (see Blasi et al. (2022)), since it is a monotone transformation of a Gaussian RF. Thus, for each combination (Gaussian vs. Sinh–arcsinh) and correlation family $\mathcal{M}_{0.5,\beta}$, $\mathcal{WM}_{0.3,\beta}$, $\mathcal{KM}_{0.5,1.5,\beta}$, we estimate the parameter vector $\boldsymbol{\theta} = (\mu, \sigma^2, \beta)^\top$ for the Gaussian case and $\boldsymbol{\theta} = (\mu, \sigma^2, \beta, \eta, \chi)^\top$ for the Sinh–arcsinh case. Estimation is carried out by WCLP as in (35), using the nearest–neighbor weights (36) with $m = 2$. More importantly, standard errors, CLAIC and prediction error measures are computed using a parametric bootstrap, relying on the STB simulators developed in Sections 3–5.

Table 4: WCLP estimates with associated standard errors (in parentheses), CLAIC, RMSE and MAE for Gaussian and Sinh–arcsinh random fields with underlying correlation functions $\mathcal{M}_{0.5,\beta}$, $\mathcal{WM}_{0.3,\beta}$ and $\mathcal{KM}_{0.5,1.5,\beta}$.

	Gaussian RF			Sinh–arcsinh RF		
	$\mathcal{M}_{0.5,\beta}$	$\mathcal{WM}_{0.3,\beta}$	$\mathcal{KM}_{0.5,1.5,\beta}$	$\mathcal{M}_{0.5,\beta}$	$\mathcal{WM}_{0.3,\beta}$	$\mathcal{KM}_{0.5,1.5,\beta}$
μ	10.5956 (0.08987)	10.5956 (0.06285)	10.5956 (0.12579)	10.80907 (0.05776)	10.80905 (0.03890)	10.80908 (0.06160)
σ^2	0.2787 (0.03243)	0.2786 (0.02929)	0.2787 (0.03628)	0.07356 (0.02020)	0.07355 (0.01873)	0.07356 (0.04393)
β	21.5686 (4.66752)	21.6678 (4.84739)	15.3546 (3.88036)	29.01005 (6.83758)	29.10862 (8.32741)	20.66545 (6.77228)
η				−0.33232 (0.08604)	−0.33231 (0.06091)	−0.33233 (0.10776)
χ				0.70912 (0.03928)	0.70913 (0.03079)	0.70912 (0.06049)
CLAIC	72325	64926	86727	−38121	−48745	−1994
RMSE	0.06911	0.06910	0.06911	0.06914	0.06914	0.06914
MAE	0.04240	0.04239	0.04240	0.04241	0.04241	0.04241

Table 4 reports WCLP estimates together with parametric-bootstrap standard errors. Overall, the estimates of the location and scale parameters are remarkably stable across correlation families.

In particular, within each marginal specification (Gaussian vs. Sinh–arcsinh), the estimates of μ and σ^2 are nearly identical for $\mathcal{M}_{0.5,\beta}$, $\mathcal{WM}_{0.3,\beta}$ and $\mathcal{KM}_{0.5,1.5,\beta}$, as expected. Likewise, for the Sinh–arcsinh models, the marginal-shape parameters η (skewness) and χ (tail heaviness) are virtually unchanged across correlation choices, indicating that these parameters are primarily informed by the marginal distribution rather than by the spatial dependence structure. The associated bootstrap standard errors support the same conclusion: differences across correlation families are minor for μ , σ^2 , η and χ , whereas the largest relative uncertainty concerns the spatial scale parameter β .

In terms of model selection, the CLAIC clearly favors the Sinh–arcsinh specification combined with the $\mathcal{WM}_{0.3,\beta}$ correlation model, which attains the lowest value among all competitors. This is consistent with the exploratory evidence in Figure 6, where the histogram suggests departures from Gaussianity. For the residuals obtained from (38), Figure 7 shows (a) a comparison between the empirical histogram and the fitted marginal model, and (b) a comparison between the empirical semivariogram and its fitted counterpart.

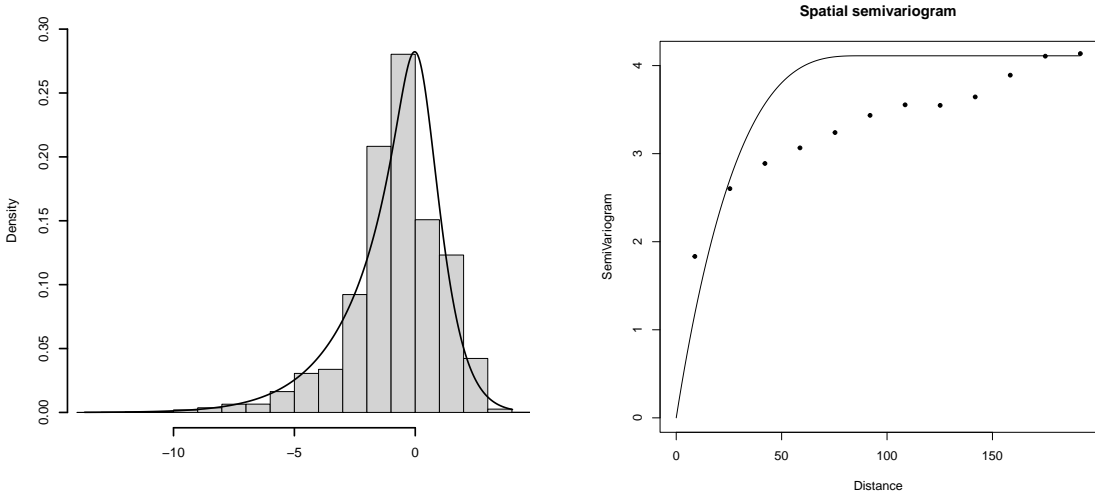


Figure 7: Residual diagnostics for the additive model (38) using the Sinh–arcsinh RF and the $\mathcal{WM}_{0.3,\beta}$ correlation model: from left to right, (a) comparison between the empirical histogram of residuals and the fitted marginal distribution, and (b) comparison between the empirical semivariogram and its fitted counterpart.

Finally, predictive accuracy is assessed on the validation set by optimal local linear kriging using 300 neighbors. The resulting RMSE and MAE are extremely similar across the three correlation models, and also differ only marginally between Gaussian and Sinh–arcsinh specifications. This lack of separation in prediction is not surprising here, since the competing correlation models share comparable smoothness and mainly differ in the tail/decay behavior of the correlation function, which appears to have limited impact on local prediction error for this dataset.

8 Conclusions

We have revisited the spectral turning–bands (STB) method as a general and scalable tool for simulating isotropic Gaussian random fields with flexible correlation structures. By exploiting probabilistic representations of the spectral measure, we derived exact STB samplers not only for the Matérn \mathcal{M} model, but also for its Kummer–Tricomi \mathcal{K} and Gauss–Hypergeometric \mathcal{GH} extensions, which allow for heavy tails, long–range dependence and compactly supported correlations, including Generalized Wendland models as special cases. These constructions lead to simple algorithms with linear computational cost in the number of locations and spectral components and are implemented in the `GeoModels` R package, making them readily applicable in large–scale simulation studies and for the generation of non–Gaussian fields via transformations of latent Gaussian processes.

A future work would be the design and fast STB simulation of multivariate random fields with \mathcal{GH} and \mathcal{K} matrix-valued covariance models, where the diagonal entries (direct covariances) quantify the spatial autocorrelations of the random field components and the off-diagonal entries (cross-covariances) their interdependence relationships. A few multivariate proposals of the former model have been presented by Daley et al. (2015) and Emery and Alegria (2022) where every direct and cross covariance belongs to the \mathcal{GH} family under specific parametric constraints, while, to best of the authors' knowledge, no study is available on multivariate \mathcal{K} models. The extension of univariate STB to the multivariate setting is not straightforward, insofar as matrix-valued covariance functions are associated with matrix-valued spectral densities that cannot be sampled as in the univariate setting; as a consequence, importance sampling strategies are often needed (Emery et al., 2016).

Acknowledgments

This work was partially funded and supported by the National Agency for Research and Development of Chile, through grants ANID FONDECYT REGULAR 1240308 (M. Bevilacqua), ANID FONDECYT INICIACION 11240330 (F. Cuevas-Pacheco) and ANID PIA CIA250010 (X. Emery).

Appendix A: Proof of the stochastic representation

Proposition 1. *Let $X \sim \Gamma(\nu, 1)$ and $Y \sim \Gamma(\alpha, 1)$ be independent, and define $T := X/Y \sim \text{BetaPrime}(\nu, \alpha)$. Let $\mathbf{Z} \sim \mathcal{N}(\mathbf{0}, I_d)$ be independent of (X, Y) and set*

$$\mathbf{Y} := \frac{1}{\beta} \frac{\mathbf{Z}}{\sqrt{T}}, \quad \beta > 0.$$

Then \mathbf{Y} is isotropic and has density

$$f_{\mathbf{Y}}(y) = \frac{\Gamma(\nu + \frac{d}{2})}{(2\pi)^{d/2} B(\alpha, \nu)} \beta^d U\left(\nu + \frac{d}{2}, 1 - \alpha + \frac{d}{2}, \frac{\beta^2 \|y\|^2}{2}\right), \quad y \in \mathbb{R}^d,$$

which coincides with the spectral density in (12).

Proof. Conditionally on $T = t > 0$, the random vector \mathbf{Y} is Gaussian with zero mean and covariance $(\beta^2 t)^{-1} I_d$, i.e.

$$\mathbf{Y} \mid T = t \sim \mathcal{N}\left(\mathbf{0}, \frac{1}{\beta^2 t} I_d\right).$$

Hence the conditional density is

$$f_{\mathbf{Y}|T}(y | t) = \frac{(\beta^2 t)^{d/2}}{(2\pi)^{d/2}} \exp\left(-\frac{\beta^2 t}{2} \|y\|^2\right),$$

which depends on y only through $\|y\|$, confirming conditional isotropy.

Since $T = X/Y$ with $X \sim \Gamma(\nu, 1)$ and $Y \sim \Gamma(\alpha, 1)$ independent, the ratio follows a Beta prime distribution (aka Beta distribution of the second kind):

$$T \sim \text{BetaPrime}(\nu, \alpha), \quad f_T(t) = \frac{t^{\nu-1}}{B(\nu, \alpha)} (1+t)^{-(\nu+\alpha)}, \quad t > 0,$$

where $B(\nu, \alpha) = \Gamma(\nu)\Gamma(\alpha)/\Gamma(\nu+\alpha)$. By the law of total probability,

$$f_{\mathbf{Y}}(y) = \int_0^\infty f_{\mathbf{Y}|T}(y | t) f_T(t) dt.$$

Setting $r = \|y\|$ and substituting the above expressions gives

$$f_{\mathbf{Y}}(y) = \frac{\beta^d}{(2\pi)^{d/2} B(\nu, \alpha)} \int_0^\infty t^{\nu+\frac{d}{2}-1} (1+t)^{-(\nu+\alpha)} \exp\left(-\frac{\beta^2 r^2}{2} t\right) dt.$$

Recall the integral representation of the confluent hypergeometric function of the second kind (Tricomi's U function):

$$U(p, q, z) = \frac{1}{\Gamma(p)} \int_0^\infty e^{-zt} t^{p-1} (1+t)^{q-p-1} dt, \quad \Re(z) > 0, \quad \Re(p) > 0.$$

Identifying parameters

$$p = \nu + \frac{d}{2}, \quad q = 1 - \alpha + \frac{d}{2}, \quad z = \frac{\beta^2 r^2}{2},$$

we observe that $q - p - 1 = -(\nu + \alpha)$, which matches the exponent in our integral. Therefore,

$$\int_0^\infty t^{\nu+\frac{d}{2}-1} (1+t)^{-(\nu+\alpha)} e^{-\frac{\beta^2 r^2}{2} t} dt = \Gamma\left(\nu + \frac{d}{2}\right) U\left(\nu + \frac{d}{2}, 1 - \alpha + \frac{d}{2}, \frac{\beta^2 r^2}{2}\right).$$

Substituting back into $f_{\mathbf{Y}}(y)$ yields

$$f_{\mathbf{Y}}(y) = \frac{\Gamma(\nu + \frac{d}{2})}{(2\pi)^{d/2} B(\nu, \alpha)} \beta^d U\left(\nu + \frac{d}{2}, 1 - \alpha + \frac{d}{2}, \frac{\beta^2 \|y\|^2}{2}\right).$$

The density depends only on $\|y\|$, confirming isotropy. Normalization follows because $f_{\mathbf{Y}}$ is obtained as the mixture of properly normalized Gaussian densities. By continuity, the expression also holds at $r = 0$ (with the limit of $U(a, b, z)$ as $z \rightarrow 0$). This completes the proof. \square

Proposition 2. *Let*

$$g_R(r | b) = C_H(\nu, d) b^d {}_1F_2\left(\delta; \delta + \frac{1}{2}, 2\delta; -(br)^2/4\right)$$

be the radial spectral density in (24). Then the distribution of $T := bR$ does not depend on b .

Proof. The density of R is $f_R(r \mid b) = |\mathbb{S}^{d-1}| r^{d-1} g_R(r \mid b)$. By the change of variables $t = br$ (so $r = t/b$ and $dr = dt/b$),

$$f_T(t) = f_R\left(\frac{t}{b} \mid b\right) \frac{1}{b} = |\mathbb{S}^{d-1}| \left(\frac{t}{b}\right)^{d-1} C_H b^d {}_1F_2\left(\delta; \delta + \frac{1}{2}, 2\delta; -\frac{t^2}{4}\right) \frac{1}{b} = |\mathbb{S}^{d-1}| t^{d-1} C_H {}_1F_2\left(\delta; \delta + \frac{1}{2}, 2\delta; -\frac{t^2}{4}\right),$$

which is independent of b . The same conclusion follows from the Bessel form in (26). \square

Proposition 3. *Let*

$$g_R^{(n)}\left(r \mid \frac{d}{2} + \nu, a\right) = C_H(\nu, d, n) a^{d+2n} r^{2n} {}_1F_2\left(\frac{d+1}{2} + \nu; \frac{d}{2} + 1 + \nu, d + 1 + 2\nu; -\frac{(ar)^2}{4}\right)$$

be the radial spectral density in (31). Then the distribution of $T := aR$ does not depend on a .

Proof. The proof is similar to that of Proposition 2 and the density of T is found to be the expression in (34). \square

References

- A. M. Yaglom. *Correlation Theory of Stationary and Related Random Functions. Volume I: Basic Results*. Springer, New York, 1987.
- R. J. Adler. *The Geometry of Random Fields*. Wiley, New York, 1981.
- D. Allard, X. Emery, C. Lacaux, and C. Lantuéjoul. Simulating space-time random fields with nonseparable Gneiting-type covariance functions. *Statistics and Computing*, 30(5):1479–1495, 2020.
- M. Armstrong, A. Galli, H. Beucher, G. Le Loc'h, D. Renard, B. Doligez, R. Eschard, and F. Geffroy. *Plurigaussian Simulations in Geosciences*. Springer, 2011.
- D. Arroyo and X. Emery. Algorithm 1013: An R implementation of a continuous spectral algorithm for simulating vector Gaussian random fields in Euclidean spaces. *ACM Transactions on Mathematical software*, 47(1):8, 2021.
- S. Arya, D. M. Mount, N. S. Netanyahu, R. Silverman, and A. Y. Wu. An optimal algorithm for approximate nearest neighbor searching. *Journal of the ACM*, 45:891–923, 1998.
- B. Lindsay. Composite likelihood methods. *Contemporary Mathematics*, 80:221–239, 1988.
- F. Bachoc, M. Bevilacqua, and D. Velandia. Composite likelihood estimation for a gaussian process under fixed domain asymptotics. *Journal of Multivariate Analysis*, 174:104534, 2019.
- Y. Bai, J. Kang, and P. Song. Efficient pairwise composite likelihood estimation for spatial-clustered data. *Biometrics*, 70(3):661–670, 2014. doi: 10.1111/biom.12199.
- M. Bevilacqua and C. Gaetan. Comparing composite likelihood methods based on pairs for spatial Gaussian random fields. *Statistics and Computing*, 25(5):877–892, 2015.
- M. Bevilacqua, T. Faouzi, R. Furrer, and E. Porcu. Estimation and prediction using generalized Wendland functions under fixed domain asymptotics. *Annals of Statistics*, 47:828–856, 2019.

M. Bevilacqua, C. Caamaño-Carrillo, and C. Gaetan. On modeling positive continuous data with spatiotemporal dependence. *Environmetrics*, 31(7):e2632, 2020. doi: 10.1002/env.2632.

M. Bevilacqua, C. Caamaño-Carrillo, and E. Porcu. Unifying compactly supported and Matérn covariance functions in spatial statistics. *Journal of Multivariate Analysis*, 189:104949, 2022.

M. Bevilacqua, X. Emery, and T. Faouzi. Extending the generalized Wendland covariance model. *Electronic Journal of Statistics*, 18(2):2771 – 2797, 2024. doi: 10.1214/24-EJS2270.

M. Bevilacqua, C. Caamaño Carrillo, T. Faouzi, and X. Emery. Parsimonious compactly supported covariance models in the Gauss hypergeometric class: Identifiability, reparameterizations, and asymptotic properties. *arXiv preprint*, arXiv:2506.13646, 2025a.

M. Bevilacqua, C. Caamaño-Carrillo, V. Morales-Oñate, and Cuevas-Pacheco. F. *GeoModels: Procedures for Gaussian and Non Gaussian Geostatistical (Large) Data Analysis*, 2025b. R package version 2.2.1.

F. Blasi, C. Caamaño-Carrillo, M. Bevilacqua, and R. Furrer. A selective view of climatological data and likelihood estimation. *Spatial Statistics*, 50:100596, 2022.

G. Box and M. Muller. A note on the generation of random normal deviates. *The Annals Mathematical Statistics*, 29(2):610–611, 1958.

C. Caamaño-Carrillo, M. Bevilacqua, C. López, and V. Morales-Oñate. Nearest neighbors weighted composite likelihood based on pairs for (non-)Gaussian massive spatial data with an application to Tukey-hh random fields estimation. *Computational Statistics and Data Analysis*, 191:107887, 2024.

A. Carlstein. The use of subseries values for estimating the variance of a general statistic from a stationary sequence. *The Annals of Statistics*, 14:1171–1179, 1986.

G. Chan and A. Wood. Algorithm AS 312: An algorithm for simulating stationary Gaussian random fields. *Journal of the Royal Statistical Society. Series C*, 46(1):171–181, 1997.

A. Chernih and S. Hubert. Closed form representations and properties of the generalised Wendland functions. *Journal of Approximation Theory*, 40:17–33, 2014.

J.-P. Chilès and P. Delfiner. *Geostatistics: Modeling Spatial Uncertainty, Second Edition*. John Wiley & Sons, New York, 2012.

Y.-K. Cho, S.-Y. Chung, and H. Yun. Rational extension of the Newton diagram for the positivity of ${}_1F_2$ hypergeometric functions and Askey–Szegő problem. *Constructive Approximation*, 51(1): 49–72, 2020.

F. Cuevas, D. Allard, and E. Porcu. Fast and exact simulation of Gaussian random fields defined on the sphere cross time. *Statistics and Computing*, 30(1):187–194, 2020.

D. J. Daley, E. Porcu, and M. Bevilacqua. Classes of compactly supported covariance functions for multivariate random fields. *Stochastic Environmental Research and Risk Assessment*, 29(4): 1249–1263, 2015. ISSN 1436-3240. doi: 10.1007/s00477-014-0996-y.

A. Datta, S. Banerjee, A. O. Finley, and A. E. Gelfand. Hierarchical nearest-neighbor Gaussian process models for large geostatistical datasets. *Journal of the American Statistical Association*, 111(514):800–812, 2016.

T. Davis, editor. *Direct Methods for Sparse Linear Systems*. Society for Industrial and Applied Mathematics, Philadelphia, 2006.

L. Devroye. *Non Uniform Random Variable Generation*. Springer, New York, 1986.

C. Dietrich and Newsam, G.N. A fast and exact method for multidimensional Gaussian stochastic simulations. *Water Resources Research*, 29(8):2861–2869, 1993.

I. S. Duff, A. M. Erisman, and J. K. Reid, editors. *Direct Methods for Sparse Matrices*. Clarendon, New York, 1989.

J. Elseberg, S. Magnenat, R. Siegwart, and A. Nüchter. Comparison of nearest-neighbor-search strategies and implementations for efficient shape registration. *Journal of Software Engineering for Robotics (JOSER)*, 3(1):2–12, 2012. ISSN 2035-3928.

X. Emery. Using the Gibbs sampler for conditional simulation of Gaussian-based random fields. *Computers & Geosciences*, 33:522–537, 2007.

X. Emery. Substitution random fields with Gaussian and gamma distributions: Theory and application to a pollution data set. *Mathematical Geosciences*, 40(1):83–99, 2008.

X. Emery and A. Alegría. The Gauss hypergeometric covariance kernel for modeling second-order stationary random fields in Euclidean spaces: Its compact support, properties and spectral representation. *Stochastic Environmental Research and Risk Assessment*, 36:2819—2834, 2022.

X. Emery and C. Lantuéjoul. TBSIM: A computer program for conditional simulation of three-dimensional Gaussian random fields via the turning bands method. *Computers & Geosciences*, 32(10):1615–1628, 2006.

X. Emery, D. Arroyo, and E. Porcu. An improved spectral turning-bands algorithm for simulating stationary vector Gaussian random fields. *Stochastic Environmental Research and Risk Assessment*, 30(7):1863–1873, 2016.

X. Emery, E. Porcu, and M. Bevilacqua. Unified native spaces in kernel methods. *arXiv preprint arXiv:2501.01825*, 2025.

K.-T. Fang, Kotz, Samuel, and K.-W. Ng. *Symmetric Multivariate and Related Distributions*. Monographs on Statistics and Applied Probability. Chapman and Hall, London, 1990. ISBN 9780412317101.

X. Feng, J. Zhu, P. Lin, and M. Steen-Adams. Composite likelihood estimation for models of spatial ordinal data and spatial proportional data with zero/one values. *Environmetrics*, 25(8):571–583, 2014. doi: 10.1002/env.2306.

G. Gasper. Positive integrals of Bessel functions. *SIAM Journal of Mathematical Analysis*, 6(5):868–881, 1975.

D. Geman and S. Geman. Stochastic relaxation, Gibbs distributions and the bayesian restoration of images. *IEEE Transactions on Pattern Analysis and Machine Intelligence*, 6:721–741, 1984.

T. Gneiting. Radial positive definite functions generated by Euclid’s hat. *Journal of Multivariate Analysis*, 69(1):88–119, 1999.

T. Gneiting. Compactly supported correlation functions. *Journal of Multivariate Analysis*, 83: 493–508, 2002.

Guido Masarotto and C. Varin. Gaussian copula marginal regression. *Electronic Journal of Statistics*, 6(none):1517–1549, 2012. ISSN 1935-7524. doi: 10.1214/12-EJS721.

W. Hastings. Monte Carlo sampling methods using Markov chains and their applications. *Biometrika*, 57(1):97–109, 1970.

R. J. Hijmans, Márcia Barbosa, A. Ghosh, and A. Mandel. *geodata: Download Geographic Data*, 2023. R package version 0.5-9.

M. Katzfuss and J. Guinness. A general framework for vecchia approximations of Gaussian processes. *Statistical Science*, 36(1):124–141, 2021.

C. Lantuéjoul. *Geostatistical Simulation: Models and Algorithms*. Springer, Berlin, 2002.

F. Lindgren, H. Rue, and J. Lindström. An explicit link between Gaussian fields and Gaussian Markov random fields: the stochastic partial differential equation approach. *Journal of the Royal Statistical Society: Series B*, 73:423–498, 2011. ISSN 1467-9868.

P. Ma and A. Bhadra. Beyond Matérn: on a class of interpretable confluent hypergeometric covariance functions. *Journal of the American Statistical Association*, pages 1–14, 2022.

A. Mantoglou and J. Wilson. The turning bands method for simulation of random fields using line generation by a spectral method. *Water Resources Research*, 23(7):1379–1394, 1987.

B. Matérn. *Spatial Variation — Stochastic Models and Their Application to Some Problems in Forest Surveys and Other Sampling Investigations*. Springer, Berlin, 1986.

G. Matheron. *Les Variables Régionalisées et Leur Estimation*. Masson, Paris, 1965.

G. Matheron. The intrinsic random function and their applications. *Advances in Applied Probability*, 5:439–468, 1973.

D. Morales-Navarrete, M. Bevilacqua, C. Caamaño-Carrillo, and L. M. Castro. Modeling point referenced spatial count data: A Poisson process approach. *Journal of the American Statistical Association*, 119(545):664–677, 2024.

D. F. Morales-Navarrete, M. Bevilacqua, C. Caamaño-Carrillo, and L. M. Castro. Modeling point referenced spatial count data: A Poisson process approach. *Journal of the American Statistical Association*, 119(545):664–677, 2024. doi: 10.1080/01621459.2022.2140053.

M. Myllymäki, T. Mrkvička, P. Grabarnik, H. Seijo, and U. Hahn. Global envelope tests for spatial processes. *Journal of the Royal Statistical Society Series B: Statistical Methodology*, 79(2):381–404, 03 2016.

Patrick J. Heagerty and S. R. Lele. A composite likelihood approach to binary spatial data. *Journal of the American Statistical Association*, 93(443):1099–1111, 1998. doi: 10.2307/2669853.

D. N. Politis and J. P. Romano. Large sample confidence regions based on subsamples under minimal assumptions. *The Annals of Statistics*, 22:2031–2050, 1994.

E. Porcu, M. Bevilacqua, R. Schaback, and C. J. Oates. The Matérn model: A journey through statistics, numerical analysis and machine learning. *Statistical Science*, 39(3):469 – 492, 2024. doi: 10.1214/24-STS923.

B. D. Ripley. *Stochastic Simulation*. Wiley, New York, 1987.

R. Schaback. The missing Wendland functions. *Advances in Computational Mathematics*, 34(1):67–81, 2011.

I.-J. Schoenberg. Metric spaces and completely monotone functions. *Annals of Mathematics*, 39(4):811–841, 1938.

M. Shinozuka. Simulation of multivariate and multidimensional random processes. *The Journal of the Acoustical Society of America*, 49(1B):357–367, 1971.

M. Shinozuka and C. Jan. Digital simulation of random processes and its applications. *Journal of Sound and Vibration*, 25(1):111–128, 1972.

S. A. Sisson, Y. Fan, and M. Beaumont. *Handbook of Approximate Bayesian Computation*. CRC Press, 2018.

M. L. Stein. *Interpolation of Spatial Data. Some Theory of Kriging*. Springer, New York, 1999.

C. Varin and P. Vidoni. A note on composite likelihood inference and model selection. *Biometrika*, 92(2):519–528, 2005.

C. Varin, N. Reid, and D. Firth. An overview of composite likelihood methods. *Statistica Sinica*, 21:5–42, 2011.

A. V. Vecchia. Estimation and model identification for continuous spatial processes. *Journal of the Royal Statistical Society. Series B (Methodological)*, pages 297–312, 1988.

G. Watson. *A Treatise on the Theory of Bessel Functions*. Cambridge University Press, Cambridge, 1922.

H. Wendland. Piecewise polynomial, positive definite and compactly supported radial functions of minimal degree. *Advances in Computational Mathematics*, 4:389–396, 1995.

G. Xu and M. G. Genton. Tukey g -and- h random fields. *Journal of the American Statistical Association*, 112(519):1236–1249, 2017. doi: 10.1080/01621459.2016.1205501.

D. Yarger and A. Bhadra. Multivariate confluent hypergeometric covariance functions with simultaneous flexibility over smoothness and tail decay. *Mathematical Geosciences*, 57(5):977–1001, 2025. doi: 10.1007/s11004-025-10185-6.

A. Zammit-Mangion, Sainsbury-Dale, Matthew, and R. Huser. Neural methods for amortized inference. *Annual Review of Statistics and Its Application*, 12(1):311–335, 2025.